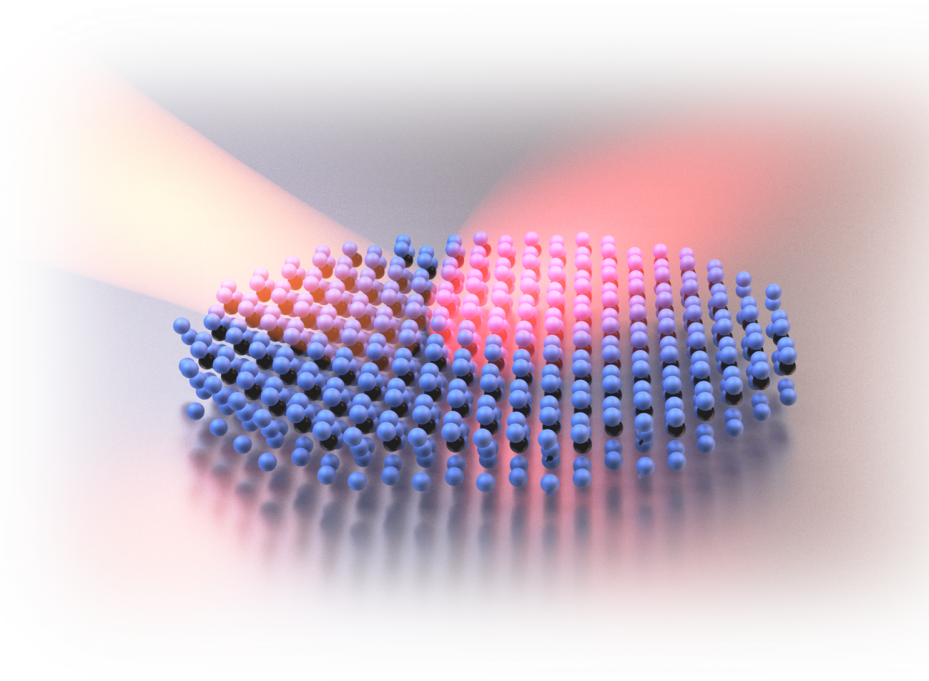




CHALMERS
UNIVERSITY OF TECHNOLOGY



Optical Properties of Transition Metal Dichalcogenide Monolayers in the vicinity of Noble Metal Surfaces

Study of Quasiparticle Physics and Strong Coupling

Master of Science in Nanotechnology

NERMIN TRNJANIN

MASTER'S THESIS 2019

Optical Properties of Transition Metal Dichalcogenide Monolayers in the vicinity of Noble Metal Surfaces

Study of Quasiparticle Physics and Strong Coupling

NERMIN TRNJANIN



CHALMERS
UNIVERSITY OF TECHNOLOGY

Department of Physics
Division of Bionanophotonics
CHALMERS UNIVERSITY OF TECHNOLOGY
Gothenburg, Sweden 2019

Optical Properties of Transition Metal Dichalcogenide Monolayers in the vicinity of
Noble Metal Surfaces
Study of Quasiparticle Physics and Strong Coupling
NERMIN TRNJANIN

© NERMIN TRNJANIN, 2019.

Supervisor: Timur Shegai, Chalmers University of Technology
Examiner: Timur Shegai, Chalmers University of Technology
Daily Supervisor: Ankit Bisht, Chalmers University of Technology
Daily Supervisor: Battulga Munkhbat, Chalmers University of Technology

Master's Thesis 2019:
Timur Shegai Group
Division of Bionanophotonics
Department of Physics
Chalmers University of Technology
SE-412 96 Gothenburg
Telephone +46 31 772 1000

Cover: Illumination and photoluminescence in a transition metal Dichalcogenide monolayer (artistic rendering D.G. Baranov, 2019).

Typeset in L^AT_EX
Printed by Chalmers Reproservice
Gothenburg, Sweden 2019

Optical Properties of Transition Metal Dichalcogenide Monolayers in the vicinity of Noble Metal Surfaces
Study of Quasiparticle Physics and Strong Coupling
NERMIN TRNJANIN
Division of Bionanophotonics
Department of Physics
Chalmers University of Technology

Abstract

In recent years strong light-matter interaction, in particular between localised plasmons and excitons in transition metal dichalcogenides (TMDCs) [1–3] has attracted great attention due to the strong oscillator strength in TMDCs [4]. The metal-TMDC interface provides a good platform to obtain strong coupling between excitons and plasmons [5]. However, this interface can affect the exciton and trion properties of TMDCs [6]. While such systems have been studied, the effect of the interface on the optical properties of the system remains an open problem.

This work has studied the changes in optical properties of TMDC monolayers due to the presence of a metal interface, with the aim to create a metal nanoparticle-TMDC platform in which the optical and excitonic modes can potentially couple strongly. Focus was put on the changes to the spectral weight of excitons and trions in the TMDCs. To realise this work, mechanically exfoliated TMDC (molybdenum disulfide(MoS_2) or tungsten disulfide(WS_2)) was used together with a metal structure, of either chemically synthesised Silver (Ag) nano-plates or top-down fabricated gold (Au) nanodisks.

Photoluminescence signals showed no significant trend in discrepancy under ambient conditions. However, a spectral shift was observed in reflection data depending on the substrate. In both photoluminescence and reflection a discrepancy was found between WS_2 -metal and WS_2 -dielectric system measurements. This contrast occurred in both ambient conditions and vacuum. The discrepancy became even clearer when the system was cooled to 77K and held at vacuum. The spectral weight was distributed among the neutral exciton and trion in the WS_2 -dielectric while the WS_2 -metal showed no trion.

When investigating the scattering of light from Au nanodisks covered by 2D WS_2 a red-shift was observed. In the case of 40 and 60 nm nanodisks a splitting in scattering spectra was also observed. This splitting can be attributed to a weak coupling between the exciton in TMDC and the plasmonic mode of the Au nanoparticle. However, more measurements are needed to confirm this result.

Keywords: **Exciton, Trion, TMDC, Interface, Spectroscopy, Photoluminescence, Nanoparticle.**

Acknowledgements

I want to express my gratitude to all the people who made this work possible. First and foremost, I would like to thank my supervisor Timur Shegai. For introducing me to the field of Nano-optics, for sharing his ideas and knowledge and for his great enthusiasm for science. His door was always open for discussions whenever issues, questions or new results arose.

I would like to thank my daily supervisors Ankit Bisht and Battulga Munkhbat. For their vast patience with someone who spends more time asking questions than listening to the answers. For teaching me the fabrication and characterisation techniques used in this work. For challenging me and forcing me to develop scientifically. I would also like to thank them for aiding me in writing this report. But most importantly for all the discussions, hard and easy lessons, inspiration and guidance through out my time at the group.

I am grateful to Luis Miguel Pais Pinto Martins, for all our talks, arguments, problem-solving, comments and Portuguese lessons.

Thanks to Denis Baranov for all the theoretical help and for re-sparking my interest in theory. I would also like to thank him for his artistic abilities. Likewise, thanks to, Adriana Canales, Michael Stühremberg, Benjamin Rousseaux and Tomasz Antosiewicz for always being open for interesting discussion and creating a great group. I also want to thank the fantastic work environment created by everyone at the Biophotonics division.

Finally, I am deeply grateful to my family, my girlfriend and my friends. Who have always been supportive and encouraged me to push on and develop.

Nermin Trnjanin, Gothenburg, March, 2019

Contents

List of Figures	xi
List of Tables	xv
1 Introduction	1
1.0.1 Aim and goals	2
1.1 Thesis Outline	3
2 Light and Matter	5
2.1 Dispersion	5
2.2 Dielectric Function	5
2.2.1 Reflection and Permittivity	6
2.2.2 Scattering and Absorption	7
2.2.2.1 Scattering and Absorption by an Oscillator	7
3 Matter and Light	9
3.1 Drude-Lorentz Model	9
3.2 Electronic Interband Transitions	9
3.2.1 Excitons	10
3.2.1.1 Frenkel Excitons	11
3.2.1.2 Wannier-Mott Excitons	11
3.2.1.3 Trion	12
3.3 Metal - Dielectric Interface	13
3.3.1 Schottky Barrier	13
3.3.2 Work Function	13
3.3.3 Light-Matter Coupling	13
3.3.4 Surface Plasmon Polaritons	14
3.3.4.1 Localised Surface Plasmons	14
3.3.5 Fluorescence near Interface	15
3.4 Transition Metal Dichalcogenides	15
4 Methods	17
4.1 Sample Fabrication	17
4.1.1 Ag Nano-Plate Fabrication	18
4.1.2 Mechanical Exfoliation	18
4.1.3 Ag - TMDC samples	19
4.1.4 Au Nanodisk - TMDC samples	19

4.2	Characterisation	20
4.2.1	Reflection	20
4.2.2	Flourescent Microscopy	21
4.2.3	Dark-Field Microscopy	21
4.2.4	Cryostat Measurements	22
4.2.5	Atomic Force Microscopy	23
4.2.6	Scanning Electron Microscopy	23
5	Results	25
5.1	Reproducibility of increase	25
5.1.1	Optical Measurements	25
5.1.1.1	Photoluminescence	25
5.1.1.2	Reflection	27
5.1.2	Topography	28
5.1.2.1	Atomic Force Microscopy	28
5.1.2.2	Scanning Electron Microscopy	30
5.2	Trion	31
5.2.1	Cryostat Measurements	31
5.3	Nanodisk Experiments	33
5.3.1	Scattering	34
5.3.1.1	Gold	34
5.3.1.2	WS ₂ on Au	35
6	Conclusions and Discussion	37
	Bibliography	41

List of Figures

3.1	Excitation of an electron and creation of a hole (and phonon) in a direct (and indirect band gap).	10
3.2	Comparison of an electron-hole pair and an exciton. Binding energy of the exciton is the difference between band gap and the exciton level.	11
3.3	A: recombination of excitons which leads to photoluminescence. B: example spectrum of photoluminescence.	11
3.4	Comparison of an exciton and a negative trion (such as in WS ₂ [7]). Binding energy of the trion is the difference between the exciton level and the trion level [8].	12
3.5	Regimes of emitter cavity coupling depicted in the energy dependence of the detuning, $\delta = \omega_c - \omega_0$. A shows the case of no coupling, the emitter decay is spontaneous. In B we see the weak coupling regime; there is a change to the energy levels but the mode splitting is not resolvable. The optical density modes of the cavity alter the emission rate (Purcell effect [9]). While in C the strong coupling regime, we can see a hybrid system with new energy levels which give an anticrossing behaviour at energy $\hbar\Omega_R$	14
3.6	A and B show hexagonal crystal structures of MoS ₂ and WS ₂ respectively. Lattice constants $a, b = 3.18 \text{ \AA}$ and $c = 18.1 \text{ \AA}$ for both approximately[10, 11].	16
3.7	A and B show optical properties of MoS ₂ while C and D shows the same for WS ₂ [10, 12]. In A and C we see the band structure of both materials with the CB in red and VB in blue. In B and D absorption spectra is seen in orange with photoluminescence in blue. Positions for two excitons X_A and X_B marked in figures B and D	16
4.1	Au markers on a 55nm SiO ₂ - Si substrate.	17
4.2	A and B show SEM images of Ag plates made using the chemical method described above. C shows an electron diffraction analysis of Ag structure. The array is characteristic of a [111] Ag facet. The crystal structure of the Ag plate was determined to be a FCC structure [13].	18
4.3	A shows bulk TMDC material on blue tape (SPV 224PR-M) being exfoliated by utilisation of shear forces. B shows another step in the process in by which the material is being transfered onto a PDSM stamp. Images taken from [14].	18

4.4	A shows a sketch of the Ag - TMDC sample. B shows a bright field image of an actual sample of MoS ₂ on a Ag plate on 55nm SiO ₂ - Si substrate.	19
4.5	A shows a sketch of the Au grid - TMDC sample. B and D are bright field images of an actual sample of WS ₂ on the Au grid on 55nm SiO ₂ - Si substrate. The luminescent part indicates the TMDC monolayer of the sample. C shows a dark field image of the same sample created by scattered light, the small dots are the Au nanodisks.	19
4.6	Illustration of the reflection measurement set up. Samples are illuminated at normal incident and reflected light is collected at normal incident and detected by a fiber-coupled spectrometer.	20
4.7	Illustration of the Photoluminescence measurement set up. Samples are illuminated at normal incident and emitted light is collected at normal incident and detected by a fiber-coupled spectrometer. A band pass filter cube is used to differentiate between illumination light and emitted light. The cube in use acts as a high-pass filter for the lamp illumination and as a Low-pass filter for the emitted light with the cut-off in both cases being 488 nm.	21
4.8	Illustration of the scattering measurement set up. Samples are illuminated at non-normal incident and emitted light is collected at normal incident and detected by a fiber-coupled spectrometer. A dark-field filter cube is used in order to ensure that scattered light is detected.	22
4.9	Set up similar to those in figures 4.6 and 4.7. Here the difference is the cryostat which is connected to a liquid nitrogen tank and a vacuum pump. The sample is illuminated and signals are detected through the sample window. A shows a configuration to measure photoluminescence and B a reflection measurement configuration.	23
5.1	A shows a bright field image of a MoS ₂ on a Ag sample. Note on the bright Ag plate, the dark yellow patches which are the MoS ₂ monolayer. The blueish part is a thicker MoS ₂ segment. In B we see a bright field image of the emitted light under blue illumination. The monolayer becomes apparent as it emits in red, the previously invisible patch on top of the Ag plate is now visible.	26
5.2	Photoluminescence signals of several samples. Each sample is represented by the colour of the line. Solid lines represent the signal taken with spot focus on a monolayer on top of Ag and the dashed lines represent the signal taken with spot focus on a monolayer on top of substrate.	26
5.3	A and B show photoluminescence signal of two samples where the signal from MoS ₂ with (solid line) and without (dashed line) Ag below, notice the peak maximum ratio between the solid and dashed signals.	27

5.4	A shows reflectance of a sample, red curve shows the reflectance of MoS ₂ on Ag and blue on the substrate. Note the spectral shift due to the substrate. B shows the contrast reflectivity in which reflectance of MoS ₂ on Ag is divided by the reflectance of MoS ₂ on the substrate. The amplitude has been offset for these curves to increase visibility. Curve obtain from sample 4 shows a weak signal and has its y-axis to the right, all others have their y-axis to the left.	28
5.5	S1 and S2 are DLSR images of the PL radiation of the respective samples. AFM as been done on five areas of interest. A (5μm × 5μm) and D (5μm × 5μm) show the MoS ₂ monolayer on the substrate . B (3.8μm × 3.8μm), E (5μm × 5μm) and F (5μm × 5μm) are AFM images om the MoS ₂ monolayer on top of Ag. D (5μm × 5μm) which shows the same area as B as well as the edge of the Ag plate.	29
5.6	Height $y(x)$ as a function of position of the four arc lengths.	30
5.7	On the left hand side, we see a SEM image of the samples used. In the middle SEM images of the same surface as in 5.5 E (top) and B (bottom). On the right hand side, SEM images of the same area as in 5.5 D (top) and A (bottom).	30
5.8	SEM images of a Ag plate. A shows a Ag plate. B shows a small Ag particle seen inside the circle of image A.	31
5.9	Reflectivity and photoluminescence signals of a sample measured under three conditions. Neutral exciton noted as X^0 and trion as X^-	32
5.10	In A one can observe the contrast in PL between a sample cleaned with oxygen plasma and not. Top of A shows signal from WS ₂ on Ag and bottom shows it on the substrate. In B reflectance is similarly compared.	33
5.11	A shows a dark field image of a Au nanodisk grid with a flake of WS ₂ placed on the upper part of the grid. B shows scattering data and fits (Gaussian) of this data for the different sizes of particles.	34
5.12	A-D (100 nm to 40 nm) show scattering data of a bare Au disk (blue), Au disk covered in WS ₂ (red) and the bare WS ₂	35
6.1	Atomic force image of a monolayer MoS ₂ [15].	38

List of Tables

4.1	Sample cleaning procedures for different sample batches.	17
5.1	Diameter of the Au nanodisks and the corresponding FWHM and peak position of their scattering data from fits (Gaussian). *Data for 40 nm was extrapolated from the data of the other particles.	34

1

Introduction

Technology which utilises light-matter interaction has been around for hundreds of years with the most basic being a simple polished mirror. In 1864 James C. Maxwell composed his equations and showed how electromagnetic waves can propagate through various media [16]. Karl F. Bruan discovers in 1874, the "unilateral conduction" between a mineral and a metal [17]. In 1894, Guglielmo Marconi builds the first successful radio wave transmitter and receiver system [18]. In the same year Jagadish C. Bose is the first to use a crystal for detection of radio waves [19]. Pickard and Braun patent a crystal detector in 1906 which consists of a crude metal-semiconductor junction, i.e. a Schottky barrier [20]. Since then there has been an explosion of technologies and devices which build upon these early inventions and utilise light-matter interaction.

The most important technologies in the 20th century have been enabled by a full understanding and mastering of a set of materials in their bulk form, although they have become much smaller. These materials are metals, insulators and semiconductors. Understanding of how these function in countless compositions have allowed us to advance in science, technology and welfare. In the 21st century, the focus has turned to 2D materials. The 2010 Nobel Prize in Physics was awarded to Andre Geim and Konstantin Novoselov "for groundbreaking experiments regarding the two-dimensional material graphene" [21]. Many have touted it as a "miracle" material.

The interest in 2D materials [22] has led to the discovery of new materials beyond the well renowned graphene, such as metals, which can be deposited as crystalline monolayers (e.g. epitaxially grown platinum). In addition other materials such as, insulators (hexagonal boron-nitride) and semiconductors including Transition metal dichalcogenides (TMDCs). These have the form MX_2 where the M is usually Mo, W and X is a chalcogenide (S, Se, Te).

Semiconductors have been crucial due to their inherent properties such as relatively small separation of the valance and conduction bands. We can chose if a semiconductor shall conduct or not by utilising a gate voltage in a transistor for example. Moreover, the optical and electronic properties of the semiconductor material in question determine how easily and extensively one can control them. TMDC materials exhibit interesting behaviour as monolayers which are very different from the bulk material, this is one of the reasons why they are of such big interest.

TMDC materials have very stable excitons (0.5-1 eV [11, 12] for monolayers) at room temperature which makes them promising for many applications. Furthermore, they transition from in-direct to direct band gap structure electrically as the material is reduced to a monolayer. Moreover, as the structure is reduced to a monolayer, the electron-hole pairs and excitons become very confined in the material and are thus very sensitive to their environment. Another interesting property is the absorbance of light in a single layer of some TMDC materials, which can be more than 10 % [4]. This makes them promising for optoelectrical applications. However, some type of metal-TMDC interface will be present in devices for application and as such it is important to understand the effect of this interface on the properties of a TMDC layer.

Interest in strong light-matter interaction, in particular between localised plasmons and excitons in TMDCs [1–3] has in recent years, attracted lots of attention due to the strong oscillator strength in TMDCs [4]. The metal-semiconductor interface is a good platform to obtain strong coupling between excitons and plasmons [5]. However, this interface can affect the exciton and trion properties of TMDCs [6]. This thesis work is focused on investigating the effect noble metal surfaces have on TMDC monolayers. In spectroscopy, this work shows how the presence of a metal surface changes the optical properties of TMDC materials. Optical measurements show a dependence on the underlying material. This dependence manifests itself as changes in spectral weight of excited electronic states. Furthermore, the goal is to explore the effect of a metal-TMDC interface in detail. In addition to this, create a metal nanoparticle-TMDC system in which the optical and excitonic modes can potentially couple strongly.

1.0.1 Aim and goals

The aim of this thesis as briefly discussed above is to get a deeper understanding of the metal-semiconductor interface. More specifically the interface between monolayers of TMDC material and noble metal surfaces. Furthermore, to use this understanding in order to realise a platform for strong coupling between plasmons and excitons in the metal-TMDC structure.

To achieve this the following goals have been set:

- Investigate the reproducibility of photoluminescence increase in monolayers of TMDC on Ag surfaces
- Using optical methods to concretise reasons behind the effect that Ag presence has on TMDC monolayers
- Use this understanding to fabricate and test a structure which has the potential to exhibit strong coupling

1.1 Thesis Outline

The thesis is structured in the following way:

- The topic is introduced and a brief background is given in Chapter 1 followed by the aim and goals of the thesis.
- Theory concerning light-matter interaction is introduced Chapter 2, to understand how the properties of materials are probed using light signals.
- Important solid state properties of crystalline structures are outlined in Chapter 3.
- Fabrication and characterisation methods are described in Chapter 4.
- Characterisation results are presented and discussed briefly in Chapter 5.
- An overview of the main conclusions is presented in Chapter 6 and followed by a deeper discussion of these.

2

Light and Matter

The following chapter describes light-matter interactions such as dispersion. Moreover, it describes certain properties of matter, which affect how it interacts with light, such as the dielectric function. Light-matter interactions can change several properties of the light and by utilising these changes one can use light as a probe into the properties of matter.

2.1 Dispersion

Dispersion corresponds to optical phenomena whereby the refractive index of a medium is frequency dependant. This is the case for all media besides vacuum[23]. In order to adjust for this, one must consider the atomic nature of matter and incorporate some frequency-dependant part of it. The contribution of a large number of atoms to the behaviour of an isotropic dielectric medium can be averaged. When such a medium is exposed to an applied electric field, the internal charge distribution is perturbed. This corresponds to the generation of electric dipole moments. These contribute to the total internal field of the dielectric. The resulting dipole moment per volume is called the electric polarisation \mathbf{P} . The electrical field \mathbf{E} and the polarisation \mathbf{P} are related via equation (2.1) [23, 24]

$$\mathbf{P} = \varepsilon_0 \chi_e \mathbf{E}, \quad \varepsilon = \varepsilon_0(1 + \chi_e) \quad (2.1)$$

where ε_0 is the permittivity of vacuum and χ_e is the electric susceptibility. The induced current inside the medium can be described as

$$\mathbf{J}_f = \frac{\partial \mathbf{P}}{\partial t}. \quad (2.2)$$

2.2 Dielectric Function

What we now desire is to rewrite the refractive index into a frequency dependant function which allows us to model light-matter behaviour more accurately and as such we can start from Maxwell's equations

$$\nabla \cdot \mathbf{B} = 0, \quad \nabla \times \mathbf{E} + \frac{\partial \mathbf{B}}{\partial t} = 0, \quad \nabla \cdot \mathbf{D} = \rho_f, \quad \nabla \times \mathbf{H} - \frac{\partial \mathbf{D}}{\partial t} = \mathbf{J}_f \quad (2.3)$$

The electric field \mathbf{E} is connected to the current density \mathbf{J}_f via conductivity σ

$$\mathbf{J}_f = \sigma \mathbf{E} \quad (2.4)$$

while the electric field is related to the displacement field \mathbf{D} via

$$\mathbf{D} = \varepsilon_0 \mathbf{E} + \mathbf{P} \quad (= \varepsilon_0 \varepsilon \mathbf{E}). \quad (2.5)$$

By Fourier transform of equations (2.4) and (2.5) and using equation (2.2) we can obtain the relationship between the conductivity and relative permittivity (now dielectric function), see equation (2.6) [25].

$$\varepsilon(\mathbf{k}, \omega) = 1 + \frac{i\sigma(\mathbf{k}, \omega)}{\varepsilon_0 \omega}. \quad (2.6)$$

Metal interaction with light can be simplified to a local response $\varepsilon(\mathbf{k} = 0, \omega)$. This simplification holds true as long as the wavelength of light in the material is much larger than the mean free path of the electrons in the material or the unit cell size of the material[26]. This is valid in the IR to UV range. Moreover, one can look at two cases of equation (2.6), where we consider high and low frequencies. At low frequencies ε , ω describe the response of bound charges to an external field and the contribution of free charges to the current flow respectively[25]. However, at optical frequencies the difference between free and bound charges is blurred. In a highly doped semiconductor, the response of the conduction electrons can be grouped together into σ' while the response of the valance band electrons can be grouped into a static dielectric constant $\delta\varepsilon$, leading to the dielectric function of form[26]

$$\varepsilon(\omega) = \delta\varepsilon + \frac{i\sigma'(\omega)}{\varepsilon_0 \omega}. \quad (2.7)$$

2.2.1 Reflection and Permittivity

The permittivity $\varepsilon(\omega) = \varepsilon_1(\omega) + i\varepsilon_2(\omega)$ and conductivity $\sigma(\omega) = \sigma_1(\omega) + i\sigma_2(\omega)$ of a material are in general complex functions of ω [26, 27]. At optical frequencies, $\varepsilon(\omega)$ can be probed via reflectivity and determination of the complex refractive index

$$\tilde{n}(\omega) = n(\omega) + i\kappa(\omega) \quad (2.8)$$

of the material. This is defined by $\sqrt{\varepsilon} = \tilde{n}$ and also yields

$$\begin{aligned} \varepsilon_1 &= n^2 - \kappa^2, \\ \varepsilon_2 &= 2n\kappa, \end{aligned} \quad (2.9)$$

where κ is called the extinction coefficient and determines the absorption of electromagnetic waves travelling through the material[27] and as such the imaginary part of the dielectric function $\varepsilon_2(\omega)$ governs the amount of absorption inside the material.

At normal incidence, the reflectivity coefficient $r(\omega)$ can be described by the following equation [27]:

$$\frac{\mathbf{E}}{\mathbf{E}'} \equiv r(\omega) \equiv \rho(\omega)e^{i\theta(\omega)}. \quad (2.10)$$

The amplitude $\rho(\omega)$ and the phase $\theta(\omega)$ are separated from the reflectivity coefficient. Moreover, at normal incidence reflectivity is related to the complex refractive index (2.8) as

$$r(\omega) = \frac{n + i\kappa - 1}{n + i\kappa + 1}. \quad (2.11)$$

Reflectance R is experimentally measurable and calculated as the ratio of the reflected intensity to the incidence intensity[27]

$$R = \frac{I'}{I} = r^*r = \rho^2. \quad (2.12)$$

Using the measured reflectance $R(\omega)$ and the Kramer-Kronig relations[24, 27], phase $\theta(\omega)$ of the reflected wave (which is difficult to measure) can be calculated. From this we can use equations (2.8-2.11) to obtain the complex dielectric function.

2.2.2 Scattering and Absorption

The frequency dependence of the refractive index arises as mentioned from the atomic nature of matter. Atoms can interact with incoming light in different ways depending on, among other things, the frequency of incident light. Scattering in particles can occur in two different cases, elastic and inelastic. Energy is conserved but not the directionality in the former case. While in the latter, it can affect the energy, phase and direction of light. Moreover, in cases when the energy of incident light matches the transition energy of the atom, it can be absorbed. This excitation can decay radiatively and non-radiatively[23, 24, 26, 27].

2.2.2.1 Scattering and Absorption by an Oscillator

The equation of motion for an electron with charge $-e$ under the influence of an harmonic force and electrical field $\mathbf{E}(\mathbf{x}, t)$ is

$$m(\ddot{\mathbf{x}} + \gamma\dot{\mathbf{x}} + \omega_0^2\mathbf{x}) = -e\mathbf{E}(\mathbf{x}, t) \quad (2.13)$$

where γ measures the damping force[24]. If the variation of the field is harmonic in time as $e^{-i\omega t}$ with frequency ω , the dipole moment contributed by one electron can be written as

$$\mathbf{p} = -e\mathbf{x} = \frac{e^2}{m}(\omega^2 - \omega_0^2 - i\omega\gamma)^{-1}\mathbf{E}. \quad (2.14)$$

If there are N molecules per unit volume and each has Z electrons, then instead of a single binding frequency for all, and if, there are f_j electrons per molecule with binding frequency ω_j and damping constant γ_j , then, the dielectric function is given by

$$\frac{\varepsilon(\omega)}{\varepsilon_0} = 1 + \frac{Ne^2}{\varepsilon_0 m} \sum_j f_j (\omega_j^2 - \omega^2 - i\omega_j\gamma_j)^{-1} \quad (2.15)$$

the oscillator strengths satisfy the sum rule $\sum_j f_j = Z$ where j is the principal quantum number [24].

This gives us two regions of interest, frequencies when ω and the binding frequency ω_j are close to each other and when they are not. In the first case, the imaginary part of the dielectric function will dominate and these regions are called regions of anomalous dispersion. Otherwise the real part dominates and this is called normal dispersion. If the imaginary part is positive, the electromagnetic wave will dissipate energy into the medium and if it is dominant the region is called region of resonant

absorption. The attenuation of a plane wave can be expressed in terms of the real and imaginary parts of the wave number $k = \beta + i\frac{\alpha}{2}$. The parameter α is the absorption or attenuation coefficient, the intensity of the wave decreases as $e^{-\alpha x}$ [24].

For metals and at high frequencies ($\omega \gg \omega_0$) we can approximate (2.15) to

$$\varepsilon_r(\omega) \approx 1 - \frac{\omega_p^2}{\omega^2} \quad (2.16)$$

where $\omega_p^2 = \frac{ne^2}{\varepsilon_0 m^*}$ is the plasma frequency given an effective mass[24, 25]. For frequencies well below the plasma frequency light penetrates only a short distance before it gets almost entirely reflected. However, as the frequency increases, metals start to transmit light and the reflectivity changes drastically.

For a non-relativistic with mass m and charge e bound by a restoring force $-m\omega_0^2\mathbf{x}$ we can obtain the induced force by an electrical field as

$$\mathbf{F} = -m\omega_0^2\mathbf{x} + e\boldsymbol{\varepsilon}E_0e^{i\mathbf{k}\cdot\mathbf{x}-i\omega t} \quad (2.17)$$

where E_0 is the magnitude and $\boldsymbol{\varepsilon}$ is the polarisation (unit/direction) vector of the incident electric field. Furthermore, a resistive term $m(\Gamma + \Gamma')\dot{\mathbf{x}}$ is introduced in the equation of motion to allow for radiative and non-radiative decay respectively (total decay constant or width $\Gamma_t = \Gamma + \Gamma'$). Finally, the characteristic (relaxation) time τ is inserted to get

$$\ddot{\mathbf{x}} + (\Gamma + \Gamma')\dot{\mathbf{x}} + \omega_0^2\mathbf{x} = \frac{eE_0}{m}\boldsymbol{\varepsilon}(1 - i\omega\tau). \quad (2.18)$$

The steady state solution \mathbf{x} to (2.18) and radiative power of a dipole $P = \frac{c^2k^4}{12\pi}\sqrt{\frac{\mu_0}{\varepsilon_0}}|\mathbf{p}|^2$, $\mathbf{p} = e\mathbf{x}$ can give us the scattering cross section [24]

$$\sigma_{sc} = 6\pi\lambda_0^2 \left[\frac{\omega^4\Gamma^2/\omega_0^2}{(\omega_0^2 - \omega^2) + \omega^2\Gamma_t^2} \right] \quad (2.19)$$

while the total cross section σ_t (absorption and scattering) is

$$\sigma_{sc}^{tot} = 6\pi\lambda_0^2 \left[\frac{\omega^2\Gamma(\Gamma' + \omega^2\Gamma/\omega_0^2)}{(\omega_0^2 - \omega^2) + \omega^2\Gamma_t^2} \right] \quad (2.20)$$

Here $\lambda = c/\omega_0$ is the resonance wavelength divided by 2π and resonance scattering width is $\Gamma = \omega_0^2\tau$. The scattering cross section has a resonance at $\omega = \omega_0$ at which σ_{sc} can have a maximum value of $6\pi\lambda_0^2(\Gamma/\Gamma_t)^2$ which is resonance fluorescence. The first Γ in the numerator corresponds to the incident radiation being absorbed and then this is multiplied by the width of the possible final states corresponding to elastic scattering and the absorptive process [24].

3

Matter and Light

This chapter focuses on certain properties of matter and how these are affected by its constituents. Furthermore, light-matter interactions are discussed and how light can affect the properties of matter. By considering key material properties which connect to the previous chapter such as dielectric functions but also phenomena derived from solid state physics such as electronic interband transitions and collective oscillations of electrons in metals.

3.1 Drude-Lorentz Model

In order to understand the optical properties of crystals, one must consider a proper dielectric function. Both the free and bound electrons can interact with incident light. The free electron model is covered by the Drude model (3.1) which is a rewritten form of equation (2.7) [28]

$$\varepsilon_{Drude} = 1 - \frac{\omega_p^2}{\omega^2 + i\gamma\omega} \quad (3.1)$$

where $\omega_p = \left(\frac{Ne^2}{m\varepsilon_0}\right)^{\frac{1}{2}}$ is the plasma frequency γ is the damping, N is the number of carriers per unit volume and m is the effective mass. In order to get a accurate model, we must account for the bound electrons which are described by the Lorentz model. In this case $\varepsilon = \varepsilon_{Drude} + \varepsilon_{Lorentz}$

$$\varepsilon = 1 - \frac{\omega_p^2}{\omega^2 + i\gamma\omega} + \frac{f\omega_0^2}{\omega_0^2 - \omega^2 - i\gamma_0\omega}. \quad (3.2)$$

Here, f is the oscillator strength, ω_0 the resonance frequency and γ_0 is damping [28]. Important to note is that the plasma frequency is not the same as in the Drude model. It is important to consider the fact that the Drude Lorentz model does not compensate for the forbidden gap region of non-metals. The Drude Lorentz model is most valid for metals, while for semiconductors it is enough to consider the Lorentz part [28].

3.2 Electronic Interband Transitions

The electronic properties of periodic crystals can be described using a band structure. The band structure is derived using periodic potentials with material dependent

parameters[26, 27]. In semiconductors there exists an energy gap between the highest occupied band (valence) and the lowest unoccupied band (conduction). In a given semiconductor there exists one out of two types of band gaps as seen in figure 3.1. Indirect or direct, depending on if the minima of the conduction band (CB) and the maximum of the valence band (VB) occur for the same \mathbf{k} vector. If this is the case then the band gap is direct, if not the gap is indirect. If a semiconductor with a

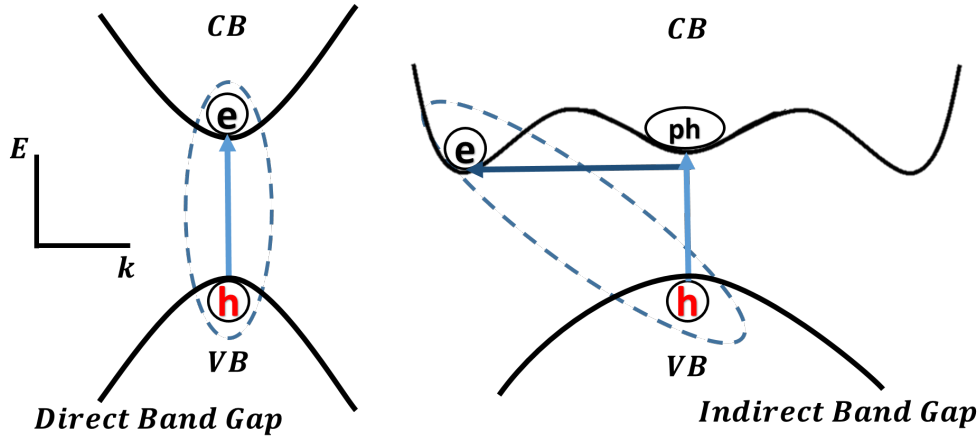


Figure 3.1: Excitation of an electron and creation of a hole (and phonon) in a direct (and indirect band gap).

direct band gap is illuminated by light (which satisfies equation (3.3)

$$\hbar\omega = E_{CB}(\mathbf{k}) - E_{VB}(\mathbf{k}), \quad (3.3)$$

where CB is an empty band and VB is a filled band), the incident light can excite an electron from the VB to the CB . For the case of an indirect band gap the incident light must generate a phonon (with energy E_{ph}) also in order to conserve momentum. In this case $\hbar\omega = E_{CB} - E_{VB} + E_{ph}$. The total absorption can be obtained by integrating over all transitions at given ω in the zone that satisfies (3.3) [27]. Transitions accumulate at frequencies for which the bands are parallel.

3.2.1 Excitons

Electron hole pairs can be created when a crystal absorbs a photon. The Coulomb interaction between the electron and hole can bind them together. Furthermore, as the electron and hole are bound they reduce their total energy thus gaining a binding energy (1 meV to 1 eV [27]). This creates a new particle called exciton. The binding energy of the excitation is illustrated in figure 3.2[26, 27]. The exciton does not transfer charge as it is neutral but it can move through the crystal and transfer energy. In addition, excitons can decay through several channels, both radiative and non-radiative. Photoluminescence is a radiative decay mode in which the electron drops into the hole and emits light characteristic to the exciton energies as in figure 3.3. There are several types of excitons and exciton complexes. The most fundamental ones are Frenkel excitons and Wannier-Mott which are outlined in this chapter. Furthermore, an important complex in this work is the trion (two

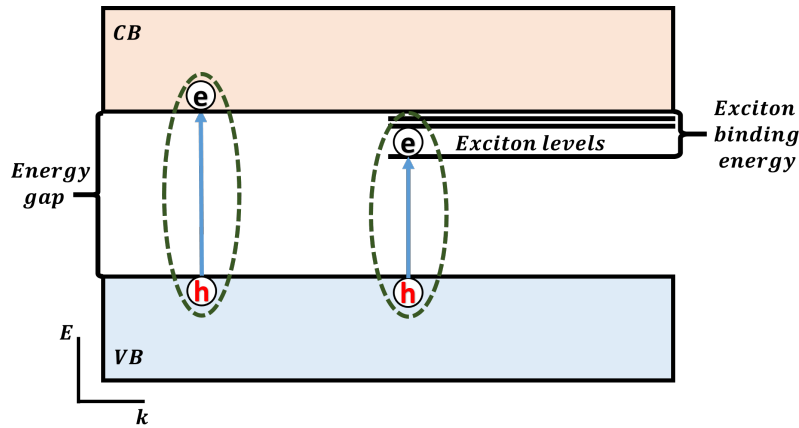


Figure 3.2: Comparison of an electron-hole pair and an exciton. Binding energy of the exciton is the difference between band gap and the exciton level.

holes and one electron or two electrons and one hole) which is discussed in more detail further down.

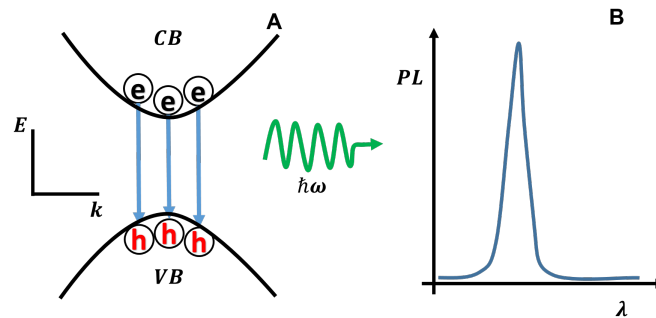


Figure 3.3: A: recombination of excitons which leads to photoluminescence. B: example spectrum of photoluminescence.

3.2.1.1 Frenkel Excitons

A Frenkel exciton is a tightly bound quasiparticle, which is usually very localised to one atom. The electron hole pair are near the same atom but the pair can hop from one atom to another by neighbour coupling [26, 27].

3.2.1.2 Wannier-Mott Excitons

The Coulomb potential between an electron in the CB and a hole in the VB, if they are weakly bound can be described as

$$U(r) = -\frac{e^2}{\epsilon r}, \quad (3.4)$$

where r is the distance between the particles and ϵ is the appropriate dielectric constant. The weakly bound exciton will have bound states which have lower total

energy than the bottom of the conduction band as shown in figure 3.2. Using a hydrogen atom model one can write the energy as a modified Rydberg equation.

$$E_n = E_g - \frac{\mu e^4}{2\hbar^2 \epsilon^2 n^2}. \quad (3.5)$$

Here n is the principal quantum number and μ is the reduced mass:

$$\frac{1}{\mu} = \frac{1}{m_e} + \frac{1}{m_h}, \quad (3.6)$$

formed from the effective masses m_e , m_h of the electron and hole. The exciton ground energy is obtained by setting $n = 1$ in (3.5) while the Bohr radius of the exciton is given by

$$a_{ex} = \frac{\epsilon \hbar^2}{\mu e^2}. \quad (3.7)$$

If the Bohr radius is reduced, changes in the parameters of equation (3.7) are such that the Wannier-Mott model will break down. If the reduction of radius is reduced enough it will form a Frenkel exciton as they are opposite extremes of the same phenomenon [26]. Typical values of the exciton Bohr radius are between 1-40 nm [7, 29].

3.2.1.3 Trion

The exciton complex trion is formed when three particle (2 holes and 1 electron or vice versa) bind together. This process happens when free electrons and excitons interact with surrounding charges and form charged excitons so called trions [8]. The formation of trions is heavily dependant of pressure and temperature as the binding energy is comparable with $k_B T$ at room temperature. Doping in semiconductor materials increases the number of charges and as such the ability of forming trions in the material. Moreover, trions can similarly to excitons decay both radiatively and non-radiatively [8, 30].

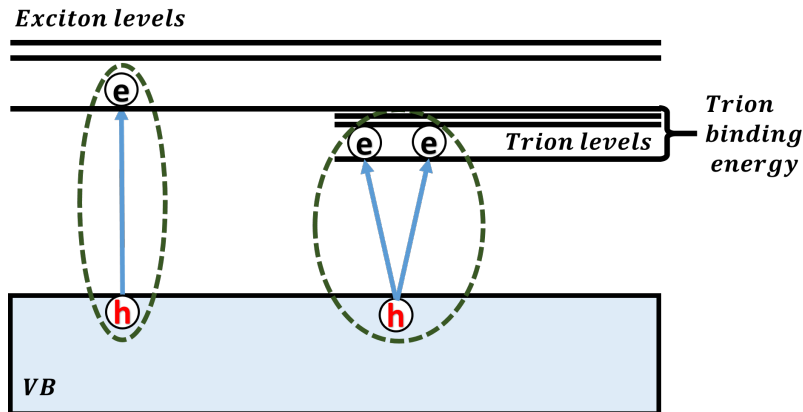


Figure 3.4: Comparison of an exciton and a negative trion (such as in WS_2 [7]). Binding energy of the trion is the difference between the exciton level and the trion level [8].

3.3 Metal - Dielectric Interface

A metal dielectric interface can affect optical and electronic phenomena in both materials in several ways, as outlined in this section.

3.3.1 Schottky Barrier

In the contact region between a metal and a semiconductor a barrier layer is formed in the semiconductor in which the charge carriers are heavily depleted. This is also called the exhaustion or depletion layer [27].

3.3.2 Work Function

The work function W of a uniform metal surface is defined as the difference in potential energy of an electron at vacuum level and Fermi level. The vacuum level is the electron energy if it is sufficiently far away from the surface, such that the electrostatic image can be ignored. The Fermi level is the electrochemical potential of the electrons in a material. The work function is affected by the symmetry and charge concentration at the exposed crystal face. The work function of a metal is at absolute zero, equal to the threshold energy for photoelectric emission. $\hbar\omega = W + T$ where $\hbar\omega$ is the energy of an incident photon, T is the kinetic energy of the emitted electron and W is the work function [27].

3.3.3 Light-Matter Coupling

If we consider a two level system interacting with a perfect optical cavity where a photon is transitioning between the two cyclically, then the dynamics of this system can be described by following Hamiltonian of Jaynes-Cummings form [5, 31, 32],

$$\mathcal{H}_{loss} = \begin{bmatrix} \omega_0 - i\gamma_0 & g \\ g & \omega_c - i\gamma_c \end{bmatrix} \quad (3.8)$$

where γ_c and γ_0 are the dissipation coefficients of the cavity and emitter while the decay width is two times these factors. Furthermore, $\hbar\omega_0$ is the transition energy of the two level system and ω_c is the resonance frequency of the cavity. The coupling strength $g = \frac{\mathbf{d}\cdot\boldsymbol{\epsilon}}{\hbar}$, where \mathbf{d} and $\boldsymbol{\epsilon}$ are the transition dipole moment and the vacuum field in the resonator at the emitter position, respectively. The coupling strength is inversely proportional to the volume of the cavity [1]. Diagonalisation of this Hamiltonian yields two eigen state energies

$$E_{\pm} = \frac{\omega_0 + \omega_c}{2} - i(\gamma_0 + \gamma_c) \pm \sqrt{g^2 + \frac{1}{4}(\delta - i(\gamma_0 - \gamma_c))^2} \quad (3.9)$$

where $\delta = \omega_c - \omega_0$ is the detuning. The Rabi splitting [5] in the case of resonance $\omega_c = \omega_0$ is $\Omega = \sqrt{4g^2 - (\gamma_0 - \gamma_c)^2}$. This gives us three cases, either $\Omega = 0$ in which case there is no coupling, $0 < 2\Omega < |\gamma_0 + \gamma_c|$ which is called the weak coupling regime where the dissipation of energy out of the coupled system is larger than the

energy transfer between the two constituents and finally $2\Omega > |\gamma_0 + \gamma_c|$ which is the strong coupling regime in which case the energy transfer outweighs any dissipation or decoherence [5, 33]. The three regimes are outlined in figure 3.5.

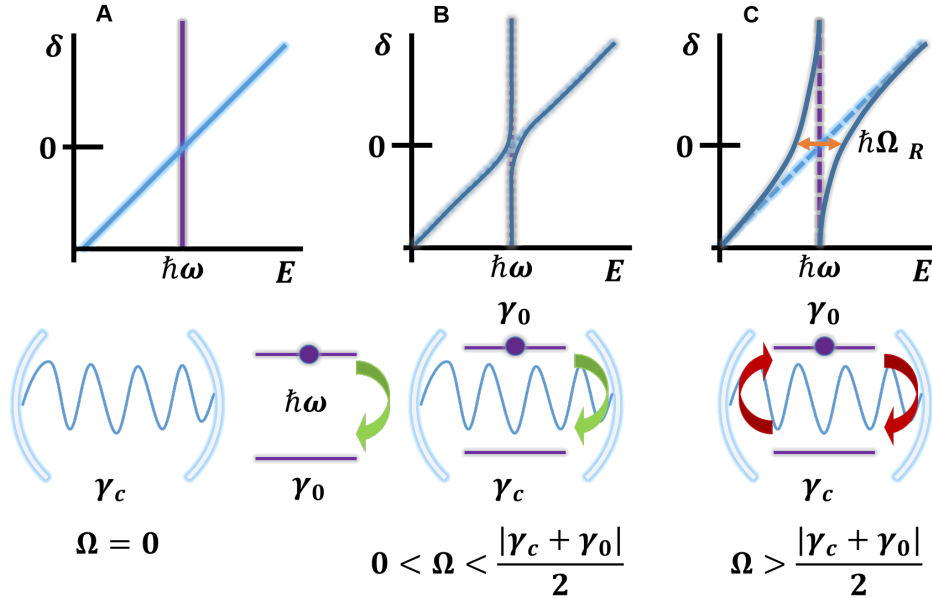


Figure 3.5: Regimes of emitter cavity coupling depicted in the energy dependence of the detuning, $\delta = \omega_c - \omega_0$. A shows the case of no coupling, the emitter decay is spontaneous. In B we see the weak coupling regime; there is a change to the energy levels but the mode splitting is not resolvable. The optical density modes of the cavity alter the emission rate (Purcell effect [9]). While in C the strong coupling regime, we can see a hybrid system with new energy levels which give an anticrossing behaviour at energy $\hbar\Omega_R$.

3.3.4 Surface Plasmon Polaritons

Surface plasmon polaritons (SPPs) are excitations propagating on the interface between a conductor and a dielectric. The SPPs are evenly confined in the perpendicular direction. SPPs arise via a coupling of the conductor's plasma to the electromagnetic oscillations [25].

3.3.4.1 Localised Surface Plasmons

Unlike SPPs, localised surface plasmons are non-propagating excitations of the conduction electrons in metallic nanostructures coupled to an oscillating electromagnetic field [25]. Solving the scattering problem of a sub-wavelength (in size) conductive nanoparticle in an oscillating electromagnetic field gives these plasmonic modes. An induced dipole moment is generated by the oscillating field which will have a resonance at a critical frequency depending on the permittivity of the nanoparticle and the surrounding medium. In the case of a spherical particle with dielectric function

ε , radius r in a surrounding non-absorbing medium with dielectric constant ε_m , the induced dipole moment is

$$\mathbf{p} = 4\pi\varepsilon_0\varepsilon_m r^3 \frac{\varepsilon - \varepsilon_m}{\varepsilon + 2\varepsilon_m} \mathbf{E}_0 \quad (3.10)$$

where \mathbf{E}_0 is the driving field. Thus the polarisability α is defined using $\mathbf{p} = \varepsilon_0\varepsilon_m\alpha\mathbf{E}_0$ as

$$\alpha = 4\pi r^3 \frac{\varepsilon - \varepsilon_m}{\varepsilon + 2\varepsilon_m} \quad (3.11)$$

which has a resonance enhancement as $|\varepsilon + 2\varepsilon_m|$ is minimised [25].

3.3.5 Fluorescence near Interface

An interface can alter the decay of an excitation in two ways. First by modifying the boundary conditions of the electromagnetic field, as such it can alter both the radiative decay rate as well as the spatial distribution of the emitted radiation. Secondly it can enhance non-radiative transfer of energy from the excited material to the interface [34]. The process of spontaneous emission such as photoluminescence is not entirely intrinsic but can be affected by external influence. The reflected field can, depending on the distance between the emitter and the interface, both enhance or quench emission. The induced mirror dipole can, depending on if it is in phase, drive the emitter. On the other hand, if it is out of phase, it can reduce the emission [34, 35]. If the distance between the emitter and the interface is varied the emission dies very quickly as the distance is reduced to very small values. This is due to coupling between the dipole field and surface plasmon polaritons. This is because the wave-vector of the mode which is in plane of the interface(metal) is always greater than that of a free photon in the medium above the emitter (air). However for emitters with low quantum yield the emission can be enhanced several orders of magnitude as a function of separation distance [36].

3.4 Transition Metal Dichalcogenides

Monolayer transition metal dichalcogenides (TMDCs) are a very interesting group of materials for several reasons. Their band gaps are in the visible and near IR regions[12], the absorption efficiency is on the order of 10% for a monolayer[10]. In addition, they transition from an indirect band gap to a direct band gap (see figures 3.7 A and C) as the material is reduced to a monolayer[11, 12]. Due to strong Coulomb interactions in the materials, the excitons are formed with binding energies in the the range of 0.5 and 1 eV [12] while the binding energy of trions is between 20 and 40 meV[30, 37]. This ensures the existence of excitons at room temperature as well as trions in some cases, and thus PL as well.

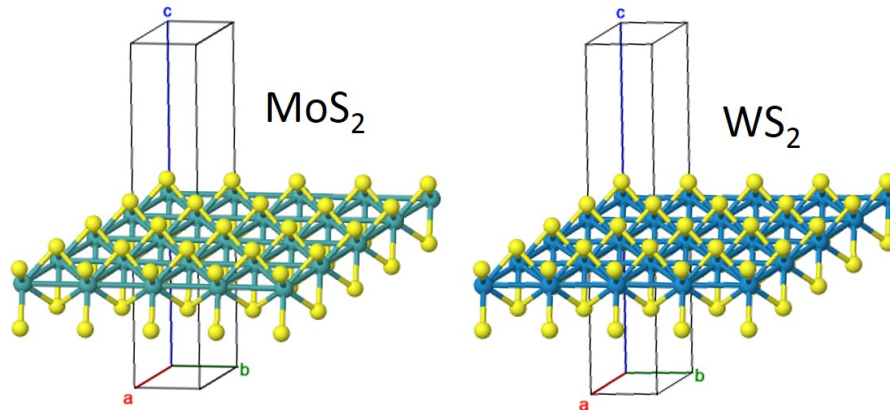


Figure 3.6: A and B show hexagonal crystal structures of MoS_2 and WS_2 respectively. Lattice constants $a, b = 3.18 \text{ \AA}$ and $c = 18.1 \text{ \AA}$ for both approximately [10, 11].

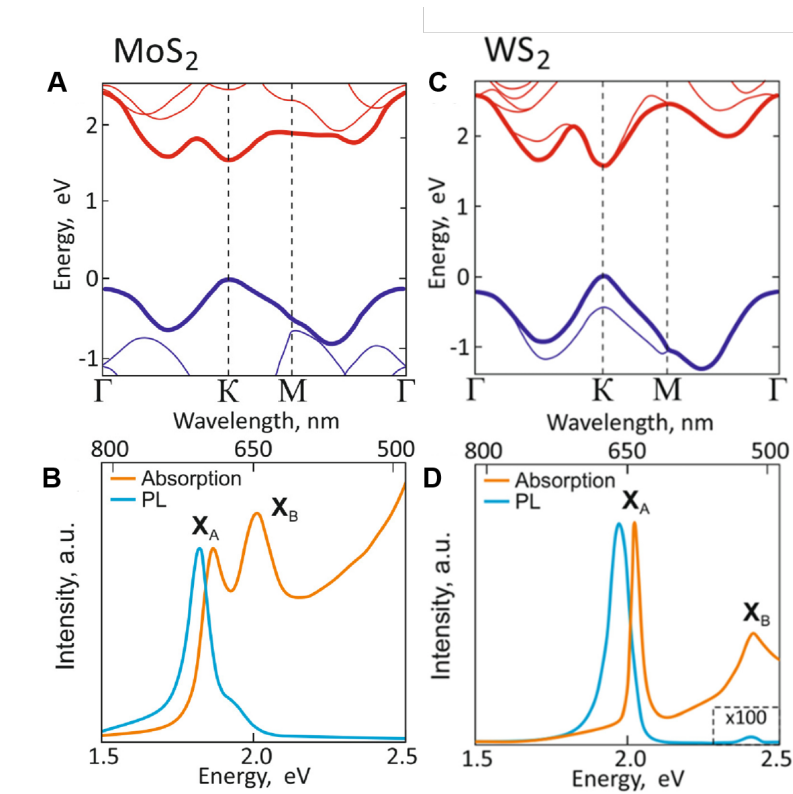


Figure 3.7: A and B show optical properties of MoS_2 while C and D shows the same for WS_2 [10, 12]. In A and C we see the band structure of both materials with the CB in red and VB in blue. In B and D absorption spectra is seen in orange with photoluminescence in blue. Positions for two excitons X_A and X_B marked in figures B and D

4

Methods

The following chapter outlines the different methods used for fabrication and characterisation of the structures used in this work. The characterisation methods are described following the explanation of sample fabrication. Experimental set-ups used for optical characterisation of samples are explained and depicted in figures in this chapter.

4.1 Sample Fabrication

This work has focused on structures containing single flakes in conjunction with metallic components such as Ag plates and Au nanodisks. This section outlines the different techniques used to fabricate some of the components of the samples. All samples used Au coated substrates consisting of a 55nm SiO₂ top layer with thick (1 mm) Si below. Substrates used for Ag samples were fabricated to have markers as in figure 4.1.

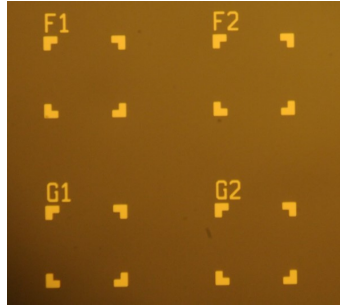


Figure 4.1: Au markers on a 55nm SiO₂ - Si substrate.

The cleaning procedures for the sample batches are outlined in table 4.1. In addition, all samples were blown dry using N₂-gas.

Sample	Acetone	IPA	Water	O ₂ -Plasma	Annealing
MoS ₂ -Ag	10min 50°C	10min 50°C	No	100W for 60s	No
WS ₂ -Ag I	7min 50°C	7min 50°C	No	50W for 60s	No
WS ₂ -Ag II	10min 60°C	10min 60°C	5min 80°C	No	No
WS ₂ -Au	No	No	No	No	10min 300°C

Table 4.1: Sample cleaning procedures for different sample batches.

4.1.1 Ag Nano-Plate Fabrication

High quality single crystalline silver plates were synthesised using a wet chemical procedure as described by [38]. Figure 4.2 A and B, show SEM images of Ag nano-plates at tilted angles of 0° and 15° with respect to the substrate, respectively. Figure 4.2 C shows the crystal structure of [111] Ag.

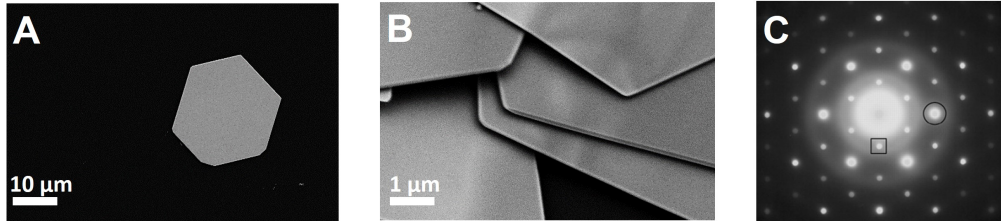


Figure 4.2: A and B show SEM images of Ag plates made using the chemical method described above. C shows an electron diffraction analysis of Ag structure. The array is characteristic of a [111] Ag facet. The crystal structure of the Ag plate was determined to be a FCC structure [13].

4.1.2 Mechanical Exfoliation

The two dimensional material is prepared via mechanical exfoliation and later transferred using the all dry method [14]. In detail the material is prepared by using scotch tape exfoliation in a clean room environment. A bulk crystal is used and a piece is exfoliated and transferred onto a polydimethylsiloxane (PDMS) sheet sitting on a glass substrate. Part of the process is depicted in figure 4.3. The sample is ready for optical inspection where flakes of the crystalline material are identified using transmission and backscattering microscopy. Once a desirable flake is identified the sample is used as a stamp. A substrate is prepared and aligned with the flake in a microscope. The glass piece and the second substrate are brought into contact using a micromanipulator and the desired flake is stamped. Using the micromanipulator the pieces are separated. The flake is inspected using transmission and backscattering microscopy.

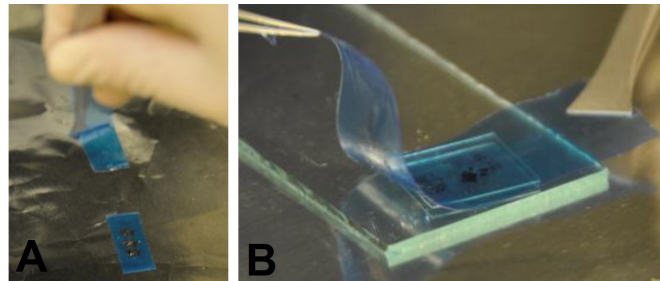


Figure 4.3: A shows bulk TMDC material on blue tape (SPV 224PR-M) being exfoliated by utilisation of shear forces. B shows another step in the process in by which the material is being transferred onto a PDMS stamp. Images taken from [14].

4.1.3 Ag - TMDC samples

Using aforementioned methods Ag plates were drop cast onto a 55nm SiO₂ - Si substrate. After drying, a monolayer of TMDC material was transferred using the dry transfer method [14] onto the plate and substrate as seen in figure 4.4.

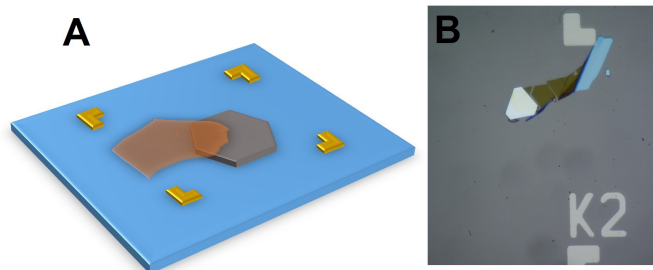


Figure 4.4: A shows a sketch of the Ag - TMDC sample. B shows a bright field image of an actual sample of MoS₂ on a Ag plate on 55nm SiO₂ - Si substrate.

4.1.4 Au Nanodisk - TMDC samples

Au nanodisks of varying size were fabricated on the same type of substrates as described above, using electron beam deposition (EBL - JEOL JBX 9300FS). These samples were cleaned and prepared as mentioned in 4.1 and vacuum sealed before a dry transfer of TMDC material was done. Sketch and finished samples are depicted in figure 4.5.

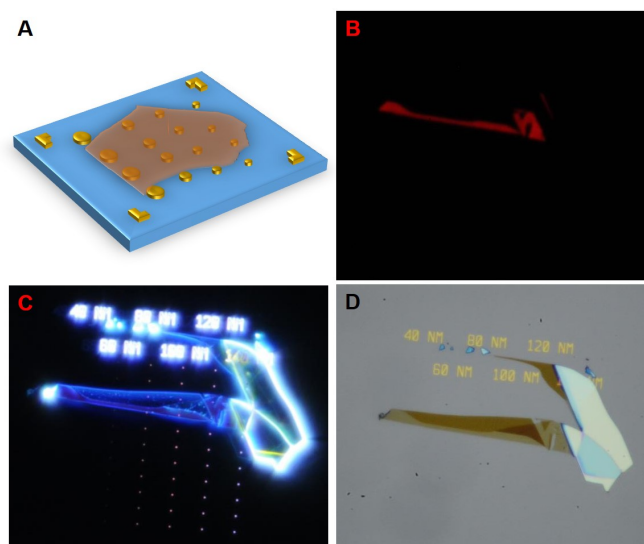


Figure 4.5: A shows a sketch of the Au grid - TMDC sample. B and D are bright field images of an actual sample of WS₂ on the Au grid on 55nm SiO₂ - Si substrate. The luminescent part indicates the TMDC monolayer of the sample. C shows a dark field image of the same sample created by scattered light, the small dots are the Au nanodisks.

4.2 Characterisation

Samples were characterised using three different techniques, extracting topography and optical properties of the samples. The main focus was put in optical measurements to extract reflectivity, scattering and fluorescence signals. These signals contain information of the fundamental optical properties of the measured samples. Moreover, topography was of interest when investigating the origin of the attributes of the aforementioned signals. Furthermore, one can assume that our Ag plates and the substrates are optically thick meaning that they will not transmit any light. As such one can assume only reflection and extinction occurs at normal incidence illumination at these surfaces.

4.2.1 Reflection

In an upright microscope, reflection is measured at normal incidence as seen in figure 4.6. Initially, the light of a halogen tungsten lamp is focused through a 50x objective (Nikon, NA=0.6) or a 20x objective (Nikon, NA=0.45) onto the surface of the sample. For such measurements, the objective NA is optimally as low as possible, such that only light reflected at near normal incidence is collected. Furthermore, the reflected light is collected by the objective and detected by a fiber-coupled spectrometer (Andor Shamrock SR-303). A thick Ag mirror was used as a reference of the reflection spectra of the lamp.

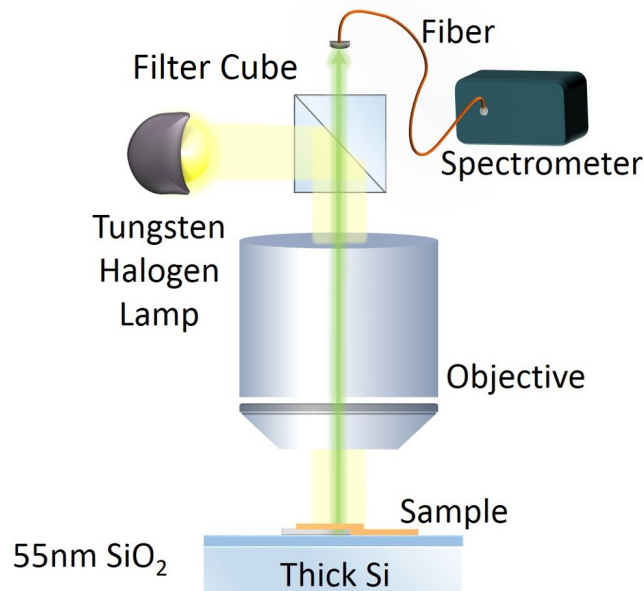


Figure 4.6: Illustration of the reflection measurement set up. Samples are illuminated at normal incident and reflected light is collected at normal incident and detected by a fiber-coupled spectrometer.

4.2.2 Fluorescent Microscopy

In an upright microscope, photoluminescence is measured at normal incidence as seen in figure 4.7. Initially, light from a white LED lamp is focused through an objective (20X, 50X or 100X; NA=0.45, NA=0.5 or NA=0.8; Nikon) onto the surface of the sample. Light is passed through a cut-off filter which only allows wavelengths equal to or shorter than 488nm to pass to the sample. Some light is absorbed and some is reflected as the sample substrate is optically thick and will not transmit. The emitted light from quasiparticle decay along with reflected light passes back through the objective towards the detector. In this direction the filter blocks any light with wavelengths equal to or shorter than 488nm. This enables us to increase the signal-to-noise ratio drastically of the photoluminescence coming from the sample. This light is then detected by a fiber-coupled spectrometer similarly to the reflection measurements.

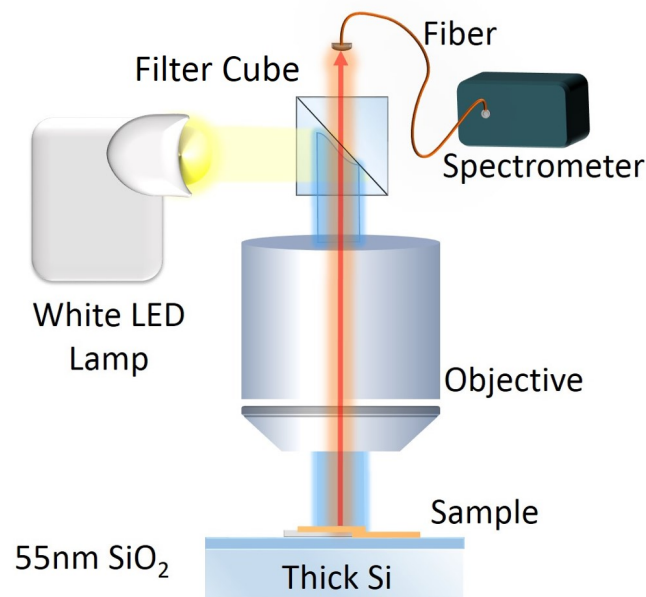


Figure 4.7: Illustration of the Photoluminescence measurement set up. Samples are illuminated at normal incident and emitted light is collected at normal incident and detected by a fiber-coupled spectrometer. A band pass filter cube is used to differentiate between illumination light and emitted light. The cube in use acts as a high-pass filter for the lamp illumination and as a Low-pass filter for the emitted light with the cut-off in both cases being 488 nm.

4.2.3 Dark-Field Microscopy

Similarly to the fluorescence and reflection measurements, dark-field microscopy was carried out using an upright microscope equipped with a dark-field filter which

consists of a blocker (filter cube) and a beam splitter as can be seen in figure 4.8. Light passes from the lamp and is reflected down towards the objective. The blocker only allows light coming in at an high angle incidence. The light interacts with the sample. The reflected light is not allowed to the detector. Scattered light which has the same angle as the illumination light is also blocked. The rest of the scattered light is collected and passed to the fiber-coupled spectrometer.

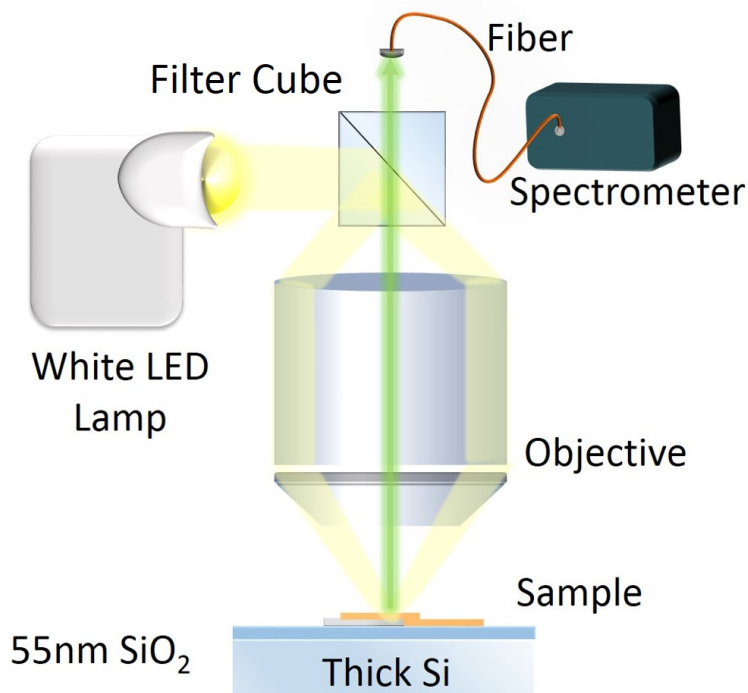


Figure 4.8: Illustration of the scattering measurement set up. Samples are illuminated at non-normal incident and emitted light is collected at normal incident and detected by a fiber-coupled spectrometer. A dark-field filter cube is used in order to ensure that scattered light is detected.

4.2.4 Cryostat Measurements

A stage was set up consisting of an upright microscope above a liquid nitrogen cooled cryostat with a vacuum. Room temperature measurements with a pressure of $\sim 10^{-5}$ Torr were conducted using this stage. Furthermore, measurements at 77K were made at a pressure of $\sim 10^{-6}$ Torr. Both reflection and fluorescence measurements were conducted in the same manner as described above. Set-ups are illustrated in figures 4.9A and 4.9B.

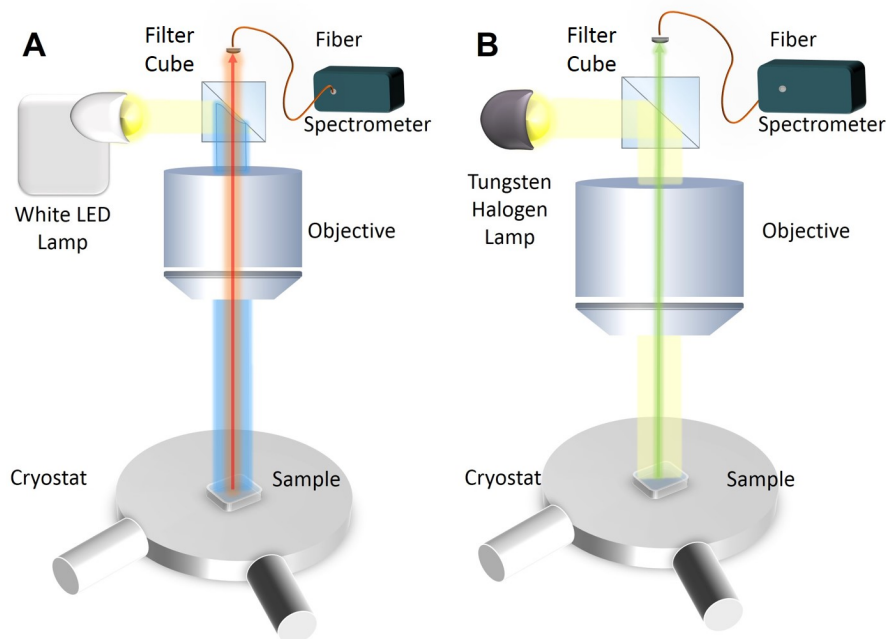


Figure 4.9: Set up similar to those in figures 4.6 and 4.7. Here the difference is the cryostat which is connected to a liquid nitrogen tank and a vacuum pump. The sample is illuminated and signals are detected through the sample window. A shows a configuration to measure photoluminescence and B a reflection measurement configuration.

4.2.5 Atomic Force Microscopy

Sample roughness was characterised with an atomic force microscope (AFM). AFM is restricted by the dimensions of the AFM-tip which will affect the resolution of the measurements. Furthermore, AFM can only provide topography and mechanical information. Measurements were done using a AFM D3100. The scans were made of $5 \times 5 \mu\text{m}^2$ areas.

4.2.6 Scanning Electron Microscopy

Scanning Electron Microscope (SEM) topography can complement AFM measurements as it provides some material information of the sample. Sample surfaces were imaged using either a JEOL JSM-6301F or a Zeiss Supra 55/60 microscope.

5

Results

The main results of this work are discussed in the following chapter, which is divided in the following sections; first the initial work which focuses on samples of MoS₂ monolayers on Ag plates. Both optical and topographical measurements were conducted and results of this work are discussed here. Moreover, TMDC material was changed to WS₂ due to its optical properties such as having a larger spectral separation between the A and B excitons . Furthermore, the radiation intensity is stronger such that signal-to-noise ratio is larger than that of MoS₂ making it visible to the naked eye reducing practical difficulties (see Section 3.4). The second section contains optical results from work on WS₂ using a cryostat set up. Finally, the last part of this chapter is focused on the Au grid with WS₂ where optical results are presented.

5.1 Reproducibility of increase

Following previous observations of relative photoluminescence increase, similar measurements were conducted in this work to investigate the reproducibility. Samples using the same materials as used in previous observations, were fabricated. The structure used was a monolayer of MoS₂ on a Ag nano-plate. The photoluminescence signal of the monolayer with focus on a spot with Ag below is compared with a signal from a spot with the SiO₂/Si substrate below. During this part of the study, seven samples were fabricated and measured, an example of these is seen in figure 5.1.

5.1.1 Optical Measurements

The optical measurements conducted in this work are those of photoluminescence and reflection. Signals representing these physical properties were mainly collected from monolayers of TMDC material with the changing parameter being the underlying material below the monolayer. The extracted data provides us with information about the extinction and radiative behaviour of the samples.

5.1.1.1 Photoluminescence

Photoluminescence (PL) signals were collected from the aforementioned samples in pairs to obtain signals from both substrates. A fiber-spot is focused on an identified patch of monolayer sitting either on the Ag plate or on top of the substrate, both of

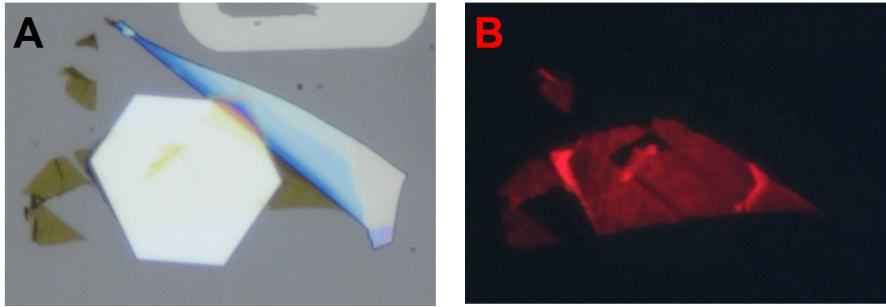


Figure 5.1: A shows a bright field image of a MoS₂ on a Ag sample. Note on the bright Ag plate, the dark yellow patches which are the MoS₂ monolayer. The blueish part is a thicker MoS₂ segment. In B we see a bright field image of the emitted light under blue illumination. The monolayer becomes apparent as it emits in red, the previously invisible patch on top of the Ag plate is now visible.

which are optically thick. Collected signals are depicted in figure 5.2 which shows a large variation in signal between samples.

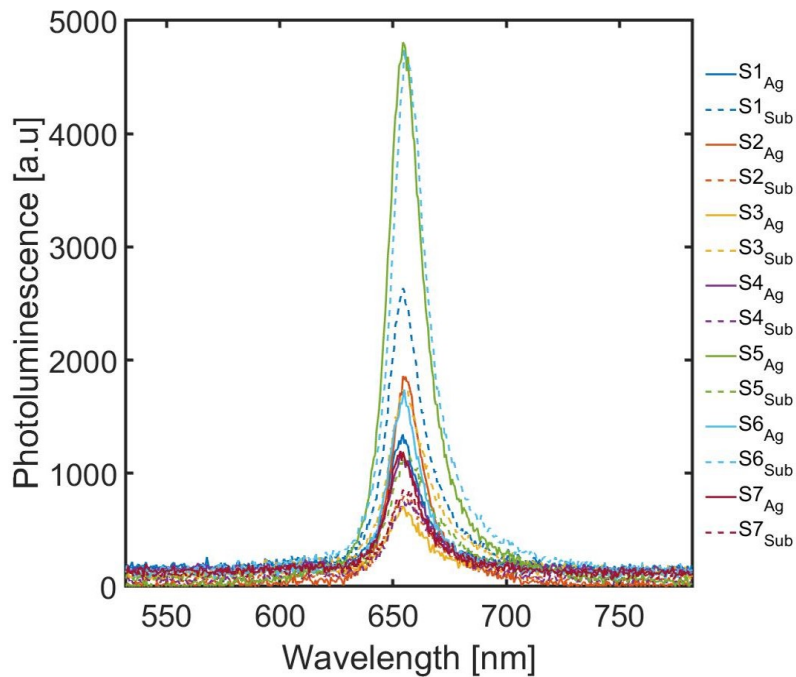


Figure 5.2: Photoluminescence signals of several samples. Each sample is represented by the colour of the line. Solid lines represent the signal taken with spot focus on a monolayer on top of Ag and the dashed lines represent the signal taken with spot focus on a monolayer on top of substrate.

Trying to estimate this variation one can look at the two extreme cases in this data-set. In figure 5.3 A we observe the largest case of negative difference photoluminescence signal when comparing monolayer on Ag with monolayer on substrate, out of these initial seven samples. The signal of the monolayer with Ag below is only

36% of the photoluminescence intensity of the same monolayer with no Ag below. Meanwhile, in figure 5.3 B one can observe the contrasting case where the Ag signal is almost five times stronger than the signal from a spot on the monolayer without Ag below. This shows an approximate range of $0.35 \times I_{MoS_2}^{Sub} \leq I_{MoS_2}^{Ag} \leq 5 \times I_{MoS_2}^{Sub}$. These results suggests that photoluminescence in presence of Ag can be stronger than photoluminescence without Ag. However, a consistent increase in PL is not entirely reproducible in this work.

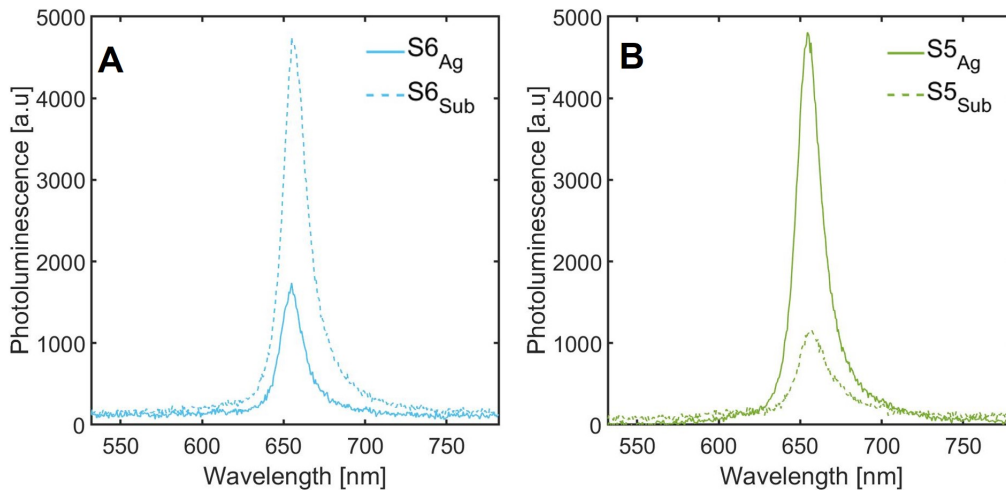


Figure 5.3: A and B show photoluminescence signal of two samples where the signal from MoS₂ with (solid line) and without (dashed line) Ag below, notice the peak maximum ratio between the solid and dashed signals.

5.1.1.2 Reflection

Besides photoluminescence measurements, reflection was also measured on the same samples. The reflection measurements indicate an interesting property, namely that the spectral positions of the dips in reflection depended on the material under the monolayer where the collection spot was focused. To illustrate this we plot $R_{MoS_2}^{Ag}$ and $R_{MoS_2}^{Sub}$ in figure 5.4 A. Furthermore, this effect is consistent throughout all samples and this is illustrated in the contrast reflectivity $R_{MoS_2}^{Ag}/R_{MoS_2}^{Sub}$ as can be seen in figure 5.4 B

$$R_{MoS_2}^{Ag} = \frac{I_{MoS_2}^{Ag} - I_{Bg}^{Ag}}{I_{Mirror}^{Ag}}, \quad R_{MoS_2}^{Sub} = \frac{I_{MoS_2}^{Sub} - I_{Bg}^{Sub}}{I_{Mirror}^{Sub}}, \quad (5.1)$$

where $I_{MoS_2}^{Ag}$ is the signal intensity from MoS₂ with Ag below, and similarly $I_{MoS_2}^{Sub}$ is the intensity from MoS₂ with no Ag below. I_{Mirror}^{Ag} is the signal of a optically thick Ag mirror which should reflect perfectly. I_{Bg}^{Ag} is the intensity of a section of the bare Ag plate and I_{Bg}^{Sub} is the intensity of a section of the bare SiO₂/Si substrate.

If the reflectance curves were only shifted in amplitude then the curves in figure 5.4 B would be flat, however as they show peaks, it indicates that there seems to be a spectral shift between the reflectivity of MoS₂ with and without Ag below. This

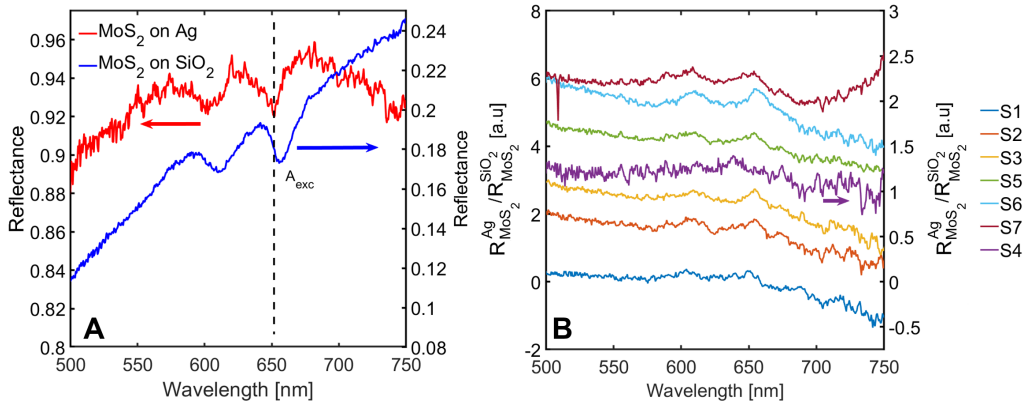


Figure 5.4: A shows reflectance of a sample, red curve shows the reflectance of MoS₂ on Ag and blue on the substrate. Note the spectral shift due to the substrate. B shows the contrast reflectivity in which reflectance of MoS₂ on Ag is divided by the reflectance of MoS₂ on the substrate. The amplitude has been offset for these curves to increase visibility. Curve obtain from sample 4 shows a weak signal and has its y-axis to the right, all others have their y-axis to the left.

shift points to the fact that Ag is consistently affecting the monolayer of TMDC material throughout all the samples. Moreover, in figure 5.4 A one can observe that the depth of the dip depends on the material under the monolayer. In order to investigate this dependence, cryostat measurements were made to investigate the presence of a charged exciton in a monolayer depending on the underlying material as its presence can change measured optical signals [6].

5.1.2 Topography

To understand what might be causing the behaviour seen in reflection measurements, topographical imaging was conducted to see if our samples match the assumptions made concerning the structure we are trying to make. To do this, two new samples were produced.

5.1.2.1 Atomic Force Microscopy

AFM scans of the two samples were made on $5\mu\text{m} \times 5\mu\text{m}$ areas using 256×256 pixels. As one can see in figure 5.5 there is a contrast between the scans of the monolayer surface depending on if Ag is below or not. When the MoS₂ layer is on the bare substrate as seen in figures 5.5 A and D, we see a much more wrinkled and irregular surface compared to the same monolayer some micron away on the Ag plate seen in figures 5.5 B, E and F. Furthermore, we see some type of spikes on the Ag surface. It is unclear what process has created them but it might be due to the dry transfer process.

Moreover, looking at figure 5.5 C we see how the monolayer slopes as it descends from the Ag plate to the bare substrate as seen in figure 5.6 which shows the topographical profiles of this area. It shows roughly that the monolayer has a 45° inclination.

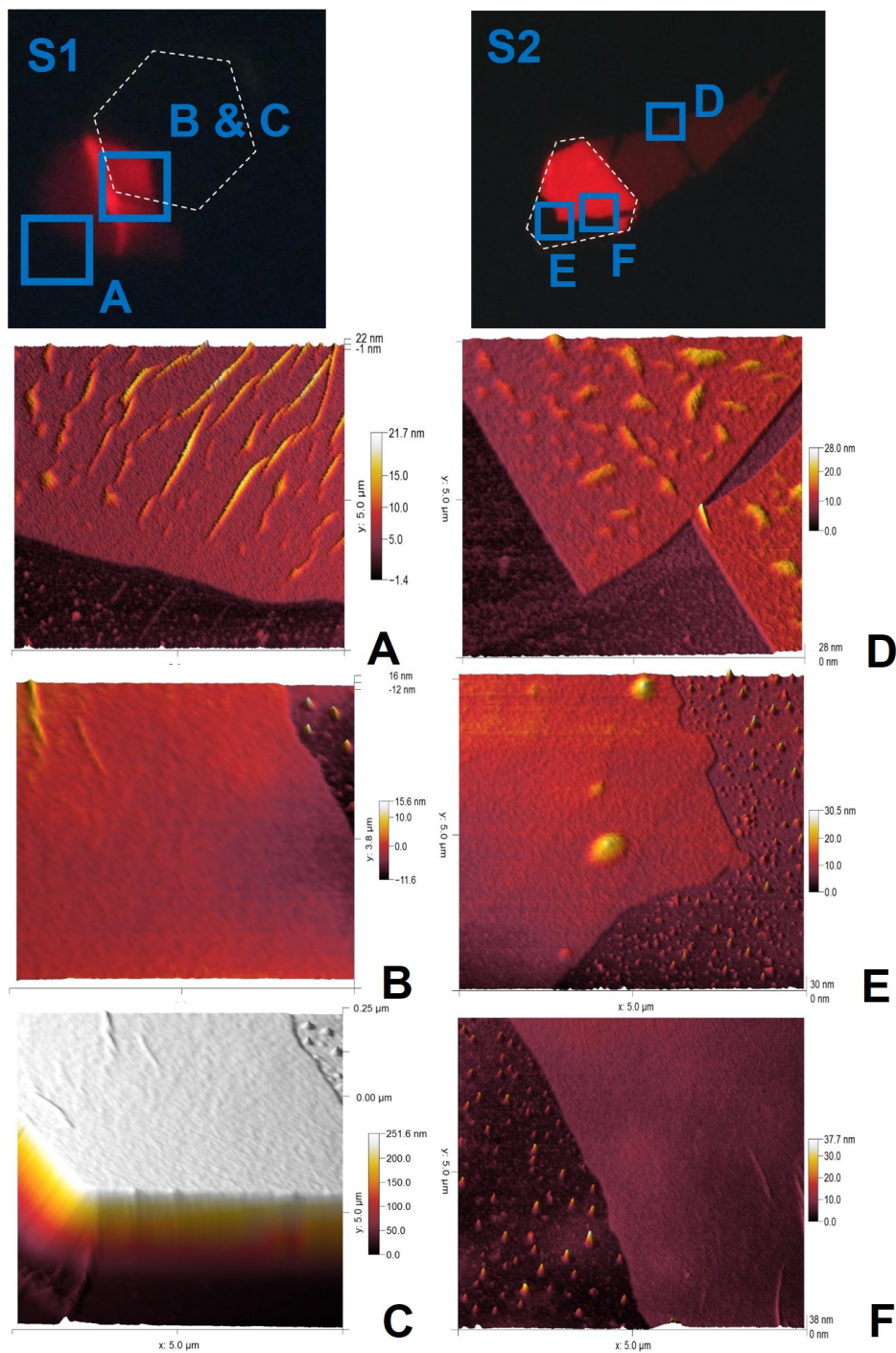


Figure 5.5: S1 and S2 are DLSR images of the PL radiation of the respective samples. AFM as been done on five areas of interest. A ($5\mu m \times 5\mu m$) and D ($5\mu m \times 5\mu m$) show the MoS₂ monolayer on the substrate. B ($3.8\mu m \times 3.8\mu m$), E ($5\mu m \times 5\mu m$) and F ($5\mu m \times 5\mu m$) are AFM images on the MoS₂ monolayer on top of Ag. D ($5\mu m \times 5\mu m$) which shows the same area as B as well as the edge of the Ag plate.

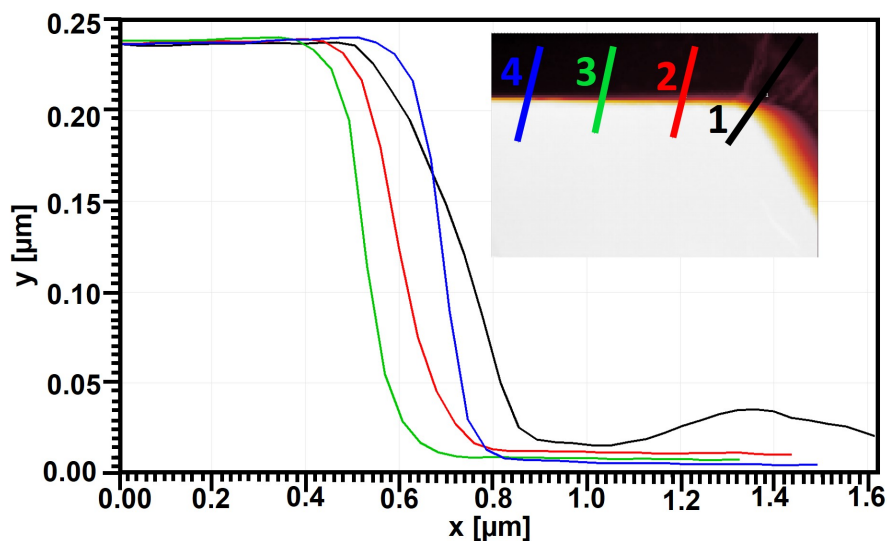


Figure 5.6: Height $y(x)$ as a function of position of the four arc lengths.

5.1.2.2 Scanning Electron Microscopy

In order to investigate the surface of the structures more thoroughly, SEM was conducted to visualise some details in them and to determine the nature of the spikes seen in the sub-figures of figure 5.5. SEM is able to resolve the conductivity of these spikes in a qualitative manner determining if they are metallic or not. However, as shown by figure 5.7 there were no bright spots indicating a metal on top of the Ag plate. There is possibly some dark shade which could indicate a organic contamination. To further ensure, a scan looking for Ag residue was made

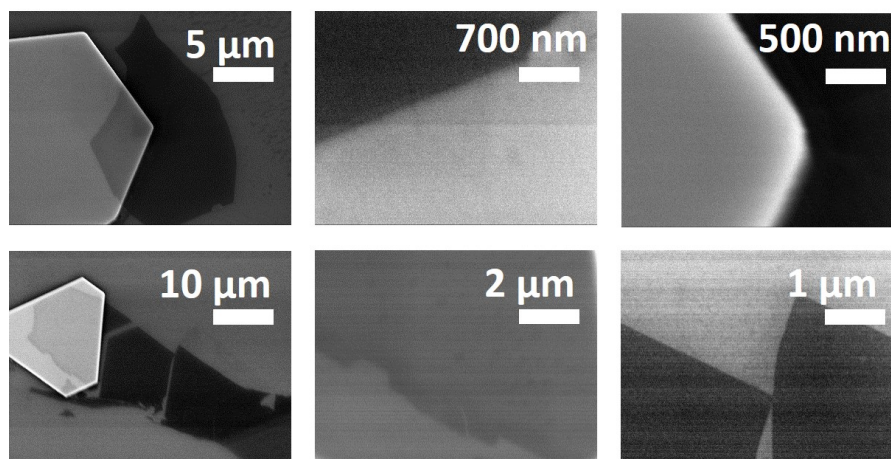


Figure 5.7: On the left hand side, we see a SEM image of the samples used. In the middle SEM images of the same surface as in 5.5 E (top) and B (bottom). On the right hand side, SEM images of the same area as in 5.5 D (top) and A (bottom).

(seen in figure 5.8). Although difficult, a piece was found and in figure 5.8 A, One can see a small piece on top of the Ag plate. More visible in figure 5.8 B. Considering

the difficulty in finding this small piece, we conclude that the Ag plates are clean and similarly to figure 4.4 we see the smoothness of these plates.

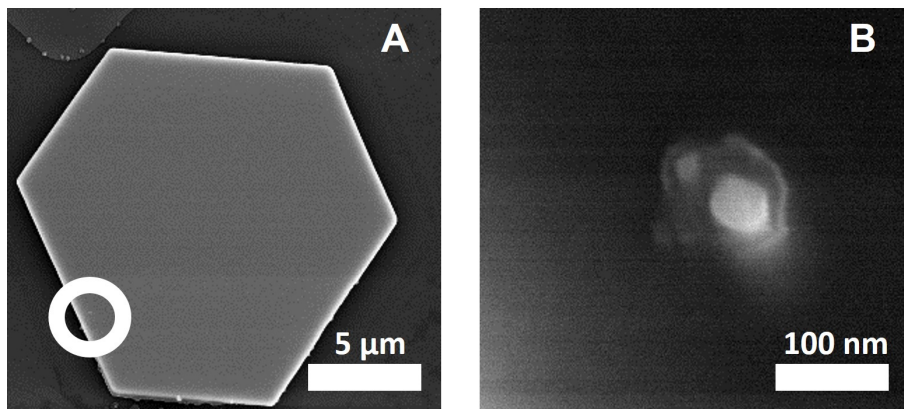


Figure 5.8: SEM images of a Ag plate. A shows a Ag plate. B shows a small Ag particle seen inside the circle of image A.

5.2 Trion

The optical data in Section 5.1.1 shows that the Ag plates are affecting the monolayer. Reflection data indicates that this effect is electrical as the reflection spectra is shifted. The stability of TMDC excitons at room temperature is quite high, while trions have a much lower binding energy (more than 10 times lower, see section 3.2.1). As such the presence of Ag should have a larger relative effect on the trion compared to the exciton. Although energetically weak, trions can still affect the radiative behaviour of TMDC monolayers. A switch from MoS₂ to WS₂ was made because the spectral weight of the trion is greater in WS₂ compared to MoS₂, and photoluminescence intensity is greater in WS₂ as well as the separation between A and B excitons as seen in figure 3.7 B and D.

5.2.1 Cryostat Measurements

Due to the fact that the trion binding energy is comparable with $k_B T$ at room temperature, reflection and photoluminescence measurements have been performed at low temperature and pressure in a cryostat configuration. Reflectance was obtained by dividing the reflection signal from the monolayer with a background signal from the underlying material ($R = I_{WS_2}^{Sub}/I_{Bq}^{Sub}$ or $R = I_{WS_2}^{Ag}/I_{Bq}^{Ag}$). This data can be seen in figure 5.9. In this experiment two parameters have been changed, the ambient temperature and the pressure in the cryostat.

In figure 5.9 A, one can observe similar photoluminescence intensity with the intensity being slightly stronger from monolayer on substrate compared to monolayer on Ag. From this figure alone, one cannot extract the effect Ag has on the monolayer. In 5.9 B we observe a new peak in photoluminescence. This arises as the trion quasiparticle decay becomes radiative. Notice that this does not occur in the Ag

signal.

Furthermore, in 5.9 C the trion photoluminescence becomes dominant in the SiO_2 signal. Under these conditions, one can also clearly observe a kink in the reflection dip which occurs around 630 nm. This is attributed to the trion as it is 30 meV from the excitation dip [39]. In all three figures of 5.9 there is no kink appearing in the reflection dip of the monolayer on Ag. Moreover, the dip appears to be symmetrical, the dip appears to be symmetrical in all three figures. This indicates that no trions are visible in this configuration. Furthermore, in 5.9 C looking at the photoluminescence spectra of monolayer on Ag we see a shoulder in the signal. The cause of this is not resolved. The results seen in

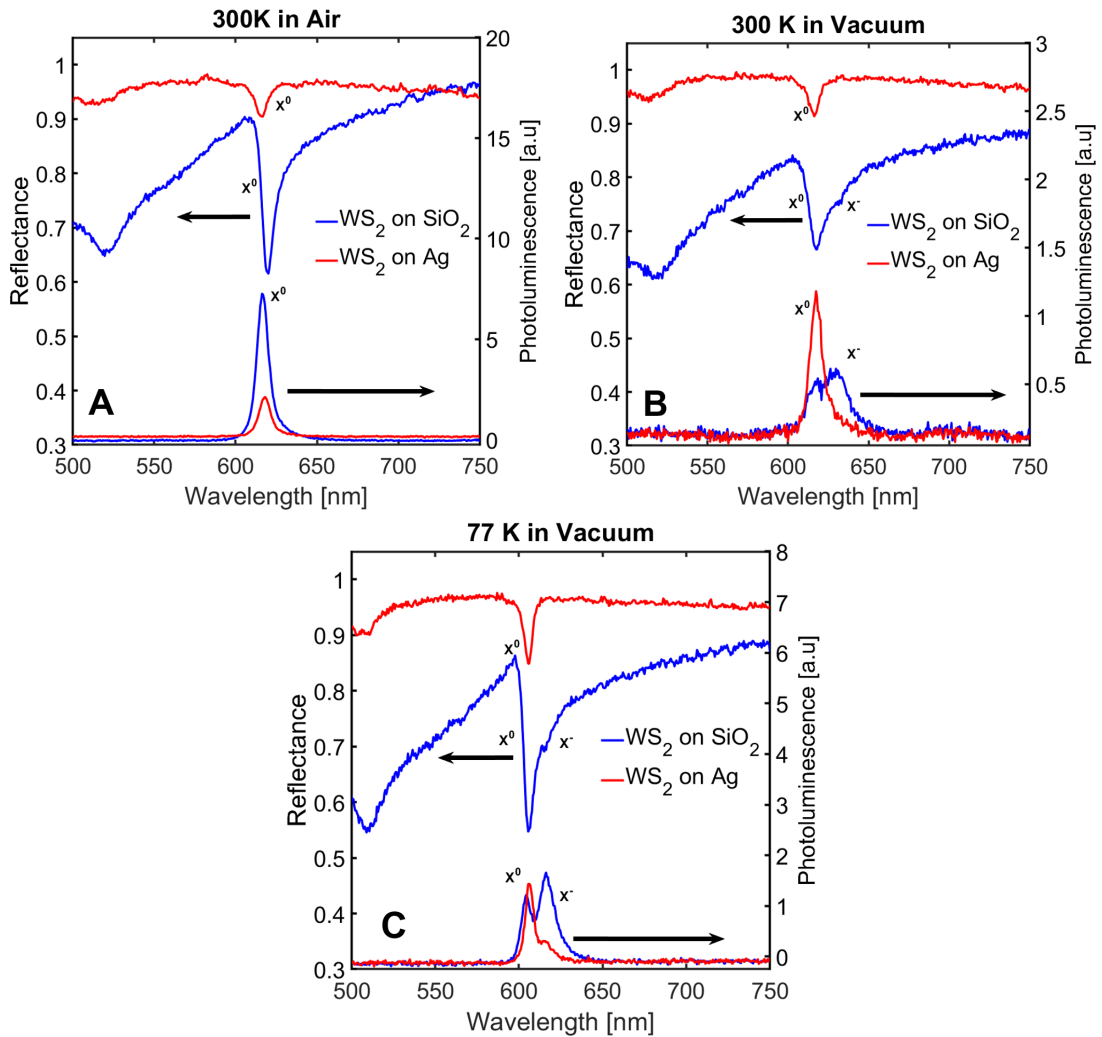


Figure 5.9: Reflectivity and photoluminescence signals of a sample measured under three conditions. Neutral exciton noted as X^0 and trion as X^- .

figure 5.9 were collected after measuring on a sample which was cleaned as outlined in table 4.1, the sample in question was marked as WS_2 -Ag I. The important factor to note is that oxygen plasma was used to clean the substrate. This might have influenced the results and caused the changes in optical behaviour of the monolayer flake. Oxygen plasma can deposit a charge on the substrate due to an enhanced

presence of ions. These ions are able to affect the photoluminescence and reflectivity of TMDC monolayers [40, 41]. In order to investigate this a new sample was prepared according to WS₂-Ag II in table 4.1. This sample was not cleaned with any oxygen plasma or ashing.

In figures 5.10 A and B, photoluminescence and reflectivity signals are compared from these two samples respectively. As one can see in figure 5.10 A, the signal coming from silver (top of figure 5.10 A) is largely unaffected. However in the bottom of figure 5.10 A, a significant difference is visible. The sample which is cleaned with oxygen plasma exhibits a larger proportion of trion photoluminescence. In the lower part of 5.10 B we see the reflectance of a monolayer on substrate. We notice that the blue curve has a well defined kink, this kink does not appear as clearly in the purple curve. This might indicate some affect which the oxygen cleaning might have. In the top part of figure 5.10 B, the signals from monolayer on top of Ag do not distinguish as much in shape. They both appear to be symmetric indicating suppression of the trion. Important to note is the slight spectral shift when comparing these two

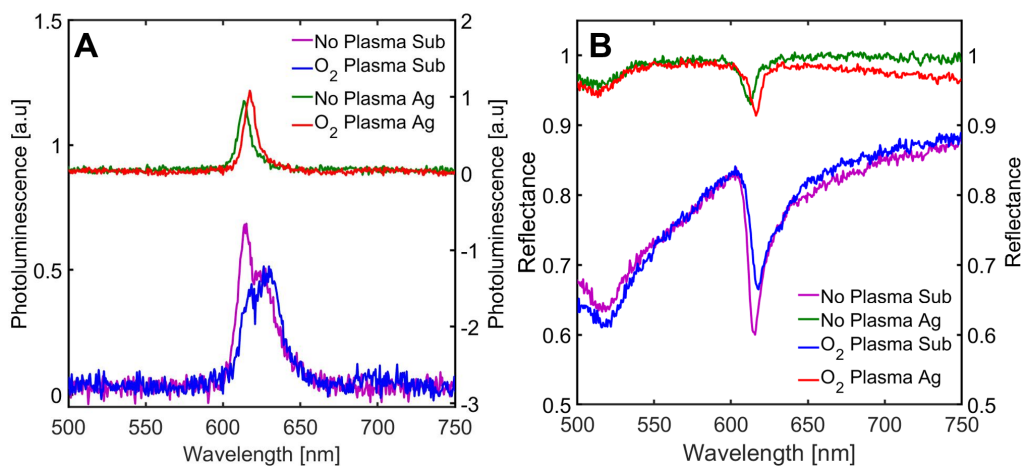


Figure 5.10: In A one can observe the contrast in PL between a sample cleaned with oxygen plasma and not. Top of A shows signal from WS₂ on Ag and bottom shows it on the substrate. In B reflectance is similarly compared.

samples. This shift could arise due to the oxygen cleaning. However, since the flake to flake variation can be quite large it is difficult to draw any conclusion about this without more data.

5.3 Nanodisk Experiments

As one can see in sections 5.1 and more specifically section 5.1.2.1 that the TMDC monolayer can appear more complex than just a layer directly on top of the substrate or Ag plate. In addition to the material below the monolayer, the quality of the interface can alter the optical and electrical behaviour of the monolayer. How large the distance is between the two layers and what lies between them affect the response of the monolayer. In order to ensure good contact between the two monolayers

some measures have been taken such as vacuum sealing the substrate containing the nanodisks. The disk sizes were varied from 40 nm in diameter to 140 nm in diameter with 20 nm increments. WS_2 was chosen as the excitonic material again because of its distinct A-exciton and greater oscillator strength in comparison to MoS_2 .

5.3.1 Scattering

In order to probe the plasmons, scattering measurements were conducted. The structure with the plasmonic Au particles can be seen in figure 5.11 A with red circles indicating the particles in question. The scattering intensities were divided by a reference intensity of Si beads $I = I_{NP}^0 / I_{Si}^{Ref}$. The scattering measurement in figure 5.11 shows the profile and resonance position of each diameter size. As the size decreases the resonance moves towards the blue.

5.3.1.1 Gold

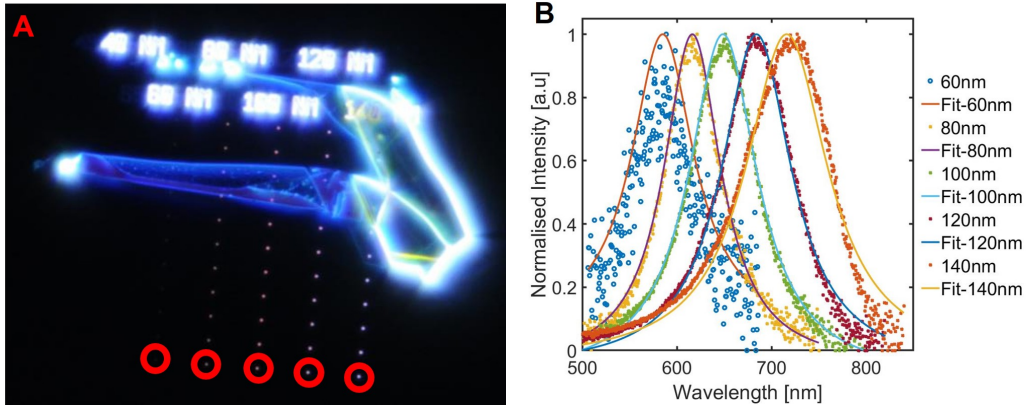


Figure 5.11: A shows a dark field image of a Au nanodisk grid with a flake of WS_2 placed on the upper part of the grid. B shows scattering data and fits (Gaussian) of this data for the different sizes of particles.

The full width half maximum (FWHM) was taken from a fit of the scattering data from each disk size which can be seen in table 5.1. From this extrapolated values were obtained for the 40 nm particle which was not visible when measuring bare Au particles.

Diameter [nm]	60	80	100	120	140	40*
FWHM [meV]	251	222	239	228	241	236*
Peak [nm]	585	616	649	684	716	554*

Table 5.1: Diameter of the Au nanodisks and the corresponding FWHM and peak position of their scattering data from fits (Gaussian). *Data for 40 nm was extrapolated from the data of the other particles.

5.3.1.2 WS₂ on Au

As one can see in figure 5.11 some particles were found under a flake of WS₂. The dimension of the flake above the particle varied from a monolayer to a multilayer. Scattering measurements of these particles are visible in figure 5.12. Signals calculated similarly to the bare nanoparticles as $I = I_{NP}^{WS_2} / I_{Si}^{Ref}$. An Au nanodisk with 100 nm diameter was found under a monolayer while 80 - 40 nm disks were all found under a multilayer of WS₂. Because of the high refractive index of WS₂ [42] the plasmon resonance is red-shifted in comparison to the bare Au particles (see equation (3.11) [25]). Moreover, one can see when comparing the different disk sizes in figures 5.12 A-D that the smaller particles show interaction. These are most likely in the weak coupling regime. The particles with sizes of 100 nm and 80 nm diameter show very little interaction. Further investigation might confirm interaction if the smaller

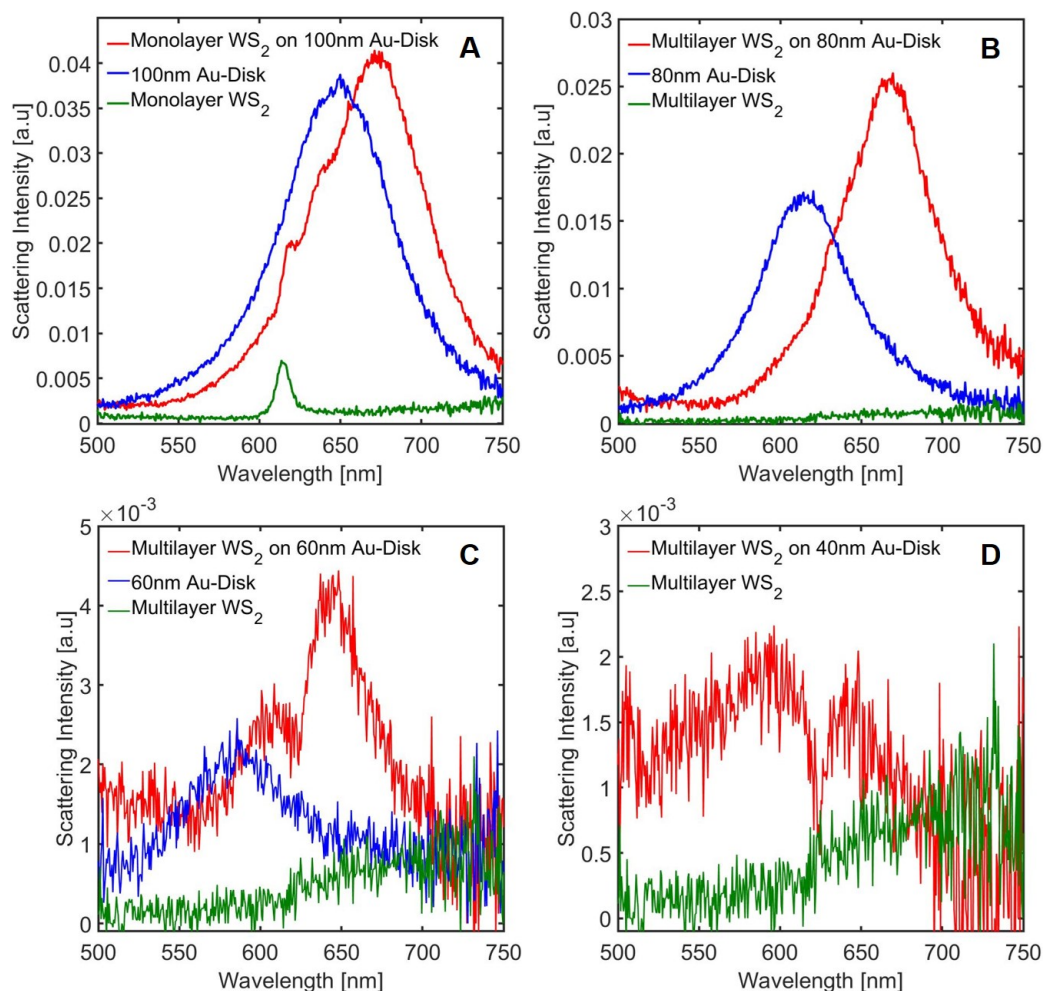


Figure 5.12: A-D (100 nm to 40 nm) show scattering data of a bare Au disk (blue), Au disk covered in WS₂ (red) and the bare WS₂.

particles could be tuned to the resonance of the excitonic material. While more time would also allow for proper fitting of the data to a proper model for coupled harmonic oscillators.

6

Conclusions and Discussion

In this thesis we have shown that:

- The reproducibility of photoluminescence increase in monolayers of TMDC on Ag surfaces was inconclusive and could not be verified.
- The effect Ag has on TMDC monolayers is a change in trion stability as it does not appear in optical measurements at 77K and vacuum.
- The noble metal-TMDC interface shows some promise for strong coupling but was not realised in this work. The weak coupling regime seems to be realised for Au nanodisks covered in a WS₂ multilayer.

There was no verification that PL is stronger in TMDC if they are on top of a metal surface. The data in Section 5.1 shows a variation. This variation can be understood by considering the effect of different decay channels and the relative enhancement and quenching of these. The nature of fluorescence is very complex and the intensity of PL can be both enhanced and quenched [34]. The resulting enhancement or quenching is due to distance (between emitter and metal surface) dependent effects which are competing. At certain distances, non-radiative enhancement is dominant, while at others radiative or absorption is enhanced [34, 36]. These effects can in particular be extreme in cases where the quantum efficiency $\frac{\Gamma_{rad}}{\Gamma_{rad} + \Gamma_{non-rad}}$ is very low (on the order of a few %); in these cases the enhancement can be of several orders of magnitude [34, 36]. Moreover, a more fair comparison could have been made, since it is difficult to estimate the quantum efficiency of TMDC flakes on the substrates used in this work. A fair comparison would be to use a reference sample which is reproducible such as freestanding TMDC [6].

In contrast to PL data, reflection data showed that the presence of Ag changed the absorption of MoS₂ and WS₂. Moreover, since it seems that there is no explanation for this change in terms of electromagnetic phenomena, the explanation must come due to a solid state physics effect. At extremely small separation, a metal-2D interface can re-normalise the band structure of the material [43]. Reducing the material from bulk to 2D removes screening effects. If you consider one electron in a TMDC material, it will be screened by all the electrons in the bulk but in 2D TMDC then one dimension is removed and as such many of the charges which induced screening [44]. Introducing the 2D to a metal surface brings it closer to a sea of electrons which can introduce screening and affect the excitons. One possible contributor of the results in this work, is how the interface affects the trion in the TMDC layer.

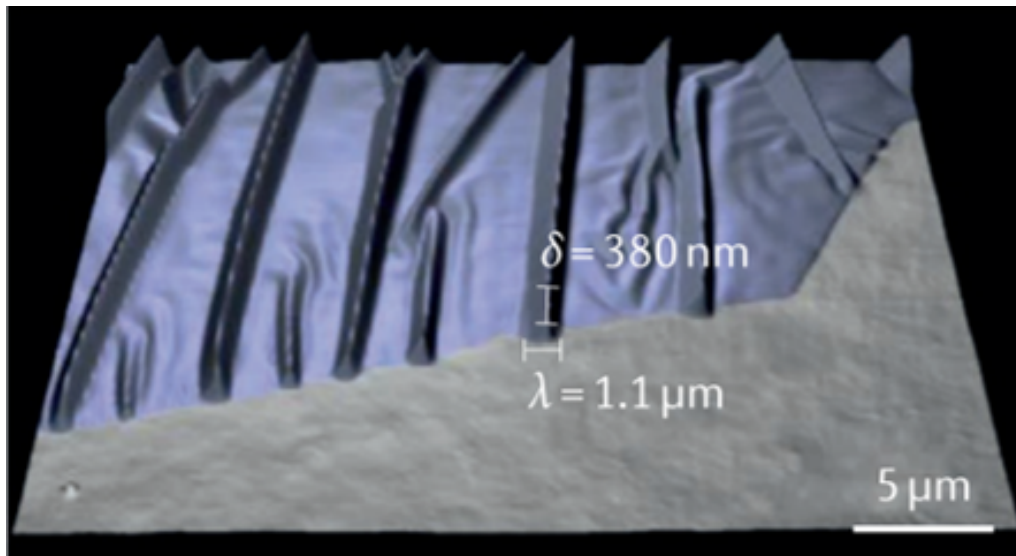


Figure 6.1: Atomic force image of a monolayer MoS₂ [15].

Substrates can redistribute the trion spectral weight [6] and this is visible in the photoluminescence.

Concerning the trion, it is very clear that there seems to be no stable trion in WS₂ on Ag at 77K and vacuum. This is clear in both PL and reflection data as seen in Section 5.2. More measurements at even lower temperature might reveal if there is at all a stable trion in this configuration. Furthermore, in figure 5.9 C, a small shoulder is visible in the Ag signal. In this work no explanation was found for this shape. This is most probably not the trion PL as it should appear in reflection data as well.

The reason for why Ag inhibits the trion is unclear. There are however, a few possible reasons, first that the binding energy of the WS₂ trion of a WS₂ layer on top of Ag is lower than k_bT at given temperatures and as such it is flushed out by heat. Moreover, there might be an electronic explanation whereby the free electrons in Ag are affecting the formation of trions in WS₂, it is important to understand that these effects are governed by Coulomb interaction and will be very sensitive to distance. If the TMDC layer is not very close to the Ag surface then Coulomb interactions might be very negligible. Furthermore, it is known that a metal-semiconductor interface will form a Schottky barrier as outlined in section 3.3.1. This is another possible way that excess charges which are needed for trion formation are being removed and thus inhibiting the formation of the particle.

What becomes clear is that constructing good contact TMDC metal interfaces is dependent on the size of the interface area [45]. AFM scans show how large area flakes buckle and wrinkle but can appear flat in segments of the area as seen in figure 6.1. One can try to combat this by shrinking the interface area from several micron squared to several nanometers squared. By doing this we can achieve a more smoother flake. A smoother flake will in turn mean that there is less variation in

distance between the metal and the 2D layer. This is important because as we previously discussed, the possible effects that the Ag surface might have on the TMDC layer are highly distance dependent.

In our attempt to utilise the experience in this work to create a platform for strong coupling showed some promise but not enough to reach the strong coupling regime (see Section 3.3.3). The results from section 5.3 showed that the smallest particles had some interaction and were most likely in the weak coupling regime. This can be attributed to size of the mode volume [1]. The results were not fit to any model and could not be analysed more than qualitatively. More thorough analysis and fabrication of reference samples would allow for more conclusive results of that system. Comparing to similar choices of materials and structures one can achieve more well defined polariton peaks and Rabi splitting in the strong coupling regime [46].

Bibliography

- [1] D.G. Baranov, Wersäll, J. M. Cuadra, T.J. Antosiewicz, and T. Shegai. Novel nanostructures and materials for strong light–matter in-teractions. *ACS Photonics*, 5:24, 2018.
- [2] Michael Stührenberg, Battulga Munkhbat, Denis G Baranov, Jorge Cuadra, Andrew B Yankovich, Tomasz J Antosiewicz, Eva Olsson, and Timur Shegai. Strong light-matter coupling between plasmons in individual gold bipyramids and excitons in mono-and multilayers of wse₂. *Nano letters*, 2018.
- [3] Ankit Bisht, Jorge Cuadra, Martin Wersäll, Adriana Canales, Tomasz J Antosiewicz, and Timur Shegai. Collective strong light-matter coupling in hierarchical microcavity-plasmon-exciton systems. *Nano letters*, 19(1):189–196, 2018.
- [4] Christian Schneider, Mikhail M Glazov, Tobias Korn, Sven Höfling, and Bernhard Urbaszek. Two-dimensional semiconductors in the regime of strong light-matter coupling. *Nature communications*, 9(1):2695, 2018.
- [5] Denis G Baranov, Martin Wersäll, Jorge Cuadra, Tomasz J Antosiewicz, and Timur Shegai. Novel nanostructures and materials for strong light–matter in-teractions. *ACS Photonics*, 5(1):24–42, 2017.
- [6] Michele Buscema, Gary A Steele, Herre SJ van der Zant, and Andres Castellanos-Gomez. The effect of the substrate on the raman and photoluminescence emission of single-layer mos₂. *Nano research*, 7(4):561–571, 2014.
- [7] Run-Ze Li, Xi-Ying Dong, Zhi-Qing Li, and Zi-Wu Wang. Correction of the exciton bohr radius in monolayer transition metal dichalcogenides. *Solid State Communications*, 275:53–57, 2018.
- [8] Akshay Singh, Galan Moody, Kha Tran, Marie E Scott, Vincent Overbeck, Gunnar Berghäuser, John Schaibley, Edward J Seifert, Dennis Pleskot, Nathaniel M Gabor, et al. Trion formation dynamics in monolayer transition metal dichalcogenides. *Physical Review B*, 93(4):041401, 2016.
- [9] Edward M Purcell, H Co Torrey, and Robert V Pound. Resonance absorption by nuclear magnetic moments in a solid. *Physical review*, 69, 1946.
- [10] Filip A Rasmussen and Kristian S Thygesen. Computational 2d materials database: electronic structure of transition-metal dichalcogenides and oxides. *The Journal of Physical Chemistry C*, 119(23):13169–13183, 2015.

- [11] Timothy C Berkelbach, Mark S Hybertsen, and David R Reichman. Theory of neutral and charged excitons in monolayer transition metal dichalcogenides. *Physical Review B*, 88(4):045318, 2013.
- [12] Alex Krasnok, Sergey Lepeshov, and Andrea Alú. Nanophotonics with 2d transition metal dichalcogenides. *Optics express*, 26(12):15972–15994, 2018.
- [13] Rongchao Jin, YunWei Cao, Chad A Mirkin, KL Kelly, George C Schatz, and JG Zheng. Photoinduced conversion of silver nanospheres to nanoprisms. *science*, 294(5548):1901–1903, 2001.
- [14] Andres Castellanos-Gomez, Michele Buscema, Rianda Molenaar, Vibhor Singh, Laurens Janssen, Herre SJ Van Der Zant, and Gary A Steele. Deterministic transfer of two-dimensional materials by all-dry viscoelastic stamping. *2D Materials*, 1(1):011002, 2014.
- [15] Sajedeh Manzeli, Dmitry Ovchinnikov, Diego Pasquier, Oleg V Yazyev, and Andras Kis. 2d transition metal dichalcogenides. *Nature Reviews Materials*, 2(8):17033, 2017.
- [16] James Clerk Maxwell. Ii. a dynamical theory of the electromagnetic field. *Proceedings of the Royal Society of London*, (13):531–536, 1864.
- [17] Ferdinand Braun. Ferdinand braun, pogg. ann., 153, p. 556, 1874. *Pogg. Ann.*, 153:556, 1874.
- [18] Prebir K Bondyopadhyay. Guglielmo marconi-the father of long distance radio communication-an engineer’s tribute. In *1995 25th European Microwave Conference*, volume 2, pages 879–885. IEEE, 1995.
- [19] Tapan K Sarkar and Dipak L Sengupta. An appreciation of jc bose’s pioneering work in millimeter waves. *IEEE Antennas and Propagation Magazine*, 39(5):55–62, 1997.
- [20] Frederick Seitz and Norman G Einspruch. First use of crystal rectifiers in wireless. *Proceedings of the American Philosophical Society*, 142(4):639–642, 1998.
- [21] Ed Gerstner. Nobel prize 2010: Andre geim & konstantin novoselov. *Nature Physics*, 6(11):836, 2010.
- [22] Andrea C Ferrari, Francesco Bonaccorso, Vladimir Fal’Ko, Konstantin S Novoselov, Stephan Roche, Peter Bøggild, Stefano Borini, Frank HL Koppens, Vincenzo Palermo, Nicola Pugno, et al. Science and technology roadmap for graphene, related two-dimensional crystals, and hybrid systems. *Nanoscale*, 7(11):4598–4810, 2015.
- [23] E. Hecht. *Optics*. Pearson education. Addison-Wesley, 2002.
- [24] John David Jackson. *Classical electrodynamics*. John Wiley and Sons, 2007.
- [25] Stefan Alexander Maier. *Plasmonics: fundamentals and applications*. Springer Science & Business Media, 2007.

-
- [26] N.W. Ashcroft and N.D. Mermin. *Solid State Physics*. HRW international editions. Holt, Rinehart and Winston, 1976.
- [27] Charles Kittel, Paul McEuen, and Paul McEuen. *Introduction to solid state physics*, volume 8. Wiley New York, 1996.
- [28] Mark Fox. *Optical properties of solids*. AAPT, 2002.
- [29] Khalil Ebrahim Jasim. Quantum dots solar cells. In *Solar Cells-New Approaches and Reviews*. IntechOpen, 2015.
- [30] Jorge Cuadra, Denis G Baranov, Martin Wersäll, Ruggero Verre, Tomasz J Antosiewicz, and Timur Shegai. Observation of tunable charged exciton polaritons in hybrid monolayer ws_2 - plasmonic nanoantenna system. *Nano letters*, 18(3):1777–1785, 2018.
- [31] Edwin T Jaynes and Frederick W Cummings. Comparison of quantum and semiclassical radiation theories with application to the beam maser. *Proceedings of the IEEE*, 51(1):89–109, 1963.
- [32] Bruce W Shore and Peter L Knight. The jaynes-cummings model. *Journal of Modern Optics*, 40(7):1195–1238, 1993.
- [33] Martin Wersäll. *Strong light-matter interactions and formation of hybrid states at the nanoscale*. Doktorsavhandlingar vid Chalmers tekniska högskola. Ny serie: 4402. Göteborg : Chalmers University of Technology, 2018., 2018.
- [34] WL Barnes. Fluorescence near interfaces: the role of photonic mode density. *journal of modern optics*, 45(4):661–699, 1998.
- [35] KH Drexhage, H Kuhn, and FP Schäfer. Variation of the fluorescence decay time of a molecule in front of a mirror. *Berichte der Bunsengesellschaft für physikalische Chemie*, 72(2):329–329, 1968.
- [36] A Wokaun, H-P Lutz, AP King, UP Wild, and RR Ernst. Energy transfer in surface enhanced luminescence. *The Journal of Chemical Physics*, 79(1):509–514, 1983.
- [37] Bairen Zhu, Xi Chen, and Xiaodong Cui. Exciton binding energy of monolayer ws_2 . *Scientific reports*, 5:9218, 2015.
- [38] Harnchana Gatemala, Prompong Pienpinijtham, Chuchaat Thammacharoen, and Sanong Ekgasit. Rapid fabrication of silver microplates under an oxidative etching environment consisting of o_2/cl^- , $\text{nh}_4\text{oh}/\text{h}_2\text{o}_2$, and h_2o_2 . *CrystEngComm*, 17(29):5530–5537, 2015.
- [39] Gerd Plechinger, Philipp Nagler, Ashish Arora, Robert Schmidt, Alexey Chernikov, Andrés Granados Del Águila, Peter CM Christianen, Rudolf Bratschitsch, Christian Schüller, and Tobias Korn. Trion fine structure and coupled spin–valley dynamics in monolayer tungsten disulfide. *Nature communications*, 7:12715, 2016.

- [40] Yuanyuan Li, Zeming Qi, Miao Liu, Yuyin Wang, Xuerui Cheng, Guobin Zhang, and Liusi Sheng. Photoluminescence of monolayer mos 2 on laalo 3 and srtio 3 substrates. *Nanoscale*, 6(24):15248–15254, 2014.
- [41] Larionette PL Mawlong, Kamal Kumar Paul, and Pravat Kumar Giri. Direct chemical vapor deposition growth of monolayer mos2 on tio2 nanorods and evidence for doping-induced strong photoluminescence enhancement. *The Journal of Physical Chemistry C*, 122(26):15017–15025, 2018.
- [42] Gwang-Hun Jung, SeokJae Yoo, and Q-Han Park. Measuring the optical permittivity of two-dimensional materials without a priori knowledge of electronic transitions. *Nanophotonics*, 8(2):263–270, 2018.
- [43] Evangelos Golias, Maxim Krivenkov, Andrei Varykhalov, Jaime Sánchez-Barriga, and Oliver Rader. Band renormalization of blue phosphorus on au (111). *Nano letters*, 18(11):6672–6678, 2018.
- [44] Alexey Chernikov, Timothy C Berkelbach, Heather M Hill, Albert Rigosi, Yilei Li, Ozgur Burak Aslan, David R Reichman, Mark S Hybertsen, and Tony F Heinz. Exciton binding energy and nonhydrogenic rydberg series in monolayer ws 2. *Physical review letters*, 113(7):076802, 2014.
- [45] Matej Velicky, Gavin E Donnelly, William R Hendren, Stephen McFarland, Declan Scullion, William JI DeBenedetti, Gabriela Calinao Correa, Yimo Han, Andrew J Wain, Melissa A Hines, et al. Mechanism of gold-assisted exfoliation of centimeter-sized transition-metal dichalcogenide monolayers. *ACS nano*, 12(10):10463–10472, 2018.
- [46] Mathias Geisler, Ximin Cui, Jianfang Wang, Tomas Rindzevicius, Lene Gammelgaard, Bjarke S Jessen, PAD Gonçalves, Francesco Todisco, Peter Bøggild, Anja Boisen, et al. Single-crystalline gold nanodisks on ws 2 mono-and multilayers: Strong coupling at room temperature. *arXiv preprint arXiv:1812.09495*, 2018.